An Evaluation of QuikSCAT UHR Wind Product's

Effectiveness in Determining

Selected Tropical Cyclone

Characteristics

Faozi Saïd

A thesis submitted to the faculty of
Brigham Young University
in partial fulfillment of the requirements for the degree of

Master of Science

David G. Long, Chair
Richard W. Christiansen
Brian D. Jeffs

Department of Electrical and Computer Engineering
Brigham Young University
December 2009

ABSTRACT

An Evaluation of QuikSCAT UHR Wind Product's

Effectiveness in Determining

Selected Tropical Cyclone

Characteristics

Faozi Saïd

Department of Electrical and Computer Engineering

Master of Science

While the standard wind product (L2B) available operationally in near-real time from SeaWinds on QuikSCAT is only 25 km in resolution, QuikSCAT data can be enhanced to yield a 2.5 km ultra-high resolution (UHR) product. The latter can be used to help estimate Tropical Cyclone (TC) characteristics such as TC eye center and wind radii. Two studies are conducted in this thesis, in which QuikSCAT UHR wind product's effectiveness in estimating these TC characteristics is evaluated. First, a comparison is made between the analyst's choice of eye location based on UHR images and interpolated best-track position. In this analysis, the UHR images are divided into two categories, based on the analyst's confidence level of finding the eye center location. In each category, statistical error quantities are computed. UHR images within the high confidence category can provide, for a given year and basin, mean error distance as small as 19 km with a 10 km standard deviation.

Second, a visual comparison of QuikSCAT's performance in estimating wind radii is made. QuikSCAT's performance is gauged against H*wind dataset and the Extended Best-Track (EBT) dataset. Results show that QuikSCAT UHR data yields a correct 34-kt wind radius most of the time regardless of the TC category when compared to both H*wind and EBT, whereas the 50- and 64-kt wind radii visual estimates do not always agree with H*wind and EBT. A more sophisticated method is also implemented to automatically estimate wind radii based on a model fit to QuikSCAT data. Results from this method are compared with EBT wind radii. Wind radii obtained from QuikSCAT model fit are generally highly correlated with EBT estimated wind radii. These two studies show that QuikSCAT UHR wind products are helpful in estimating TC eye location and wind radii, thus improving TC forecasting and analysis.

Keywords: Tropical Cyclone, QuikSCAT, eye center, wind radii, scatterometry

ACKNOWLEDGMENTS

I would like to thank David G. Long for his example, patience, and genuine interest to help students succeed. I am also grateful for all the tools (powerful computers, dedicated MERS laboratory, etc...), regular meetings, speech practices he provides for all his students. Finally, I would like to thank my wife for her patience and support during the short period of time I spent in the MERS laboratory.

Table of Contents

List of Tables

List of Figures

Chapter 1

Introduction

Weather forecasting is a challenging discipline requiring knowledge and skill to interpret and predict the earth's atmospheric behavior. One of the most dangerous atmospheric processes is a hurricane. Hurricanes are one of the most complex weather phenomena tracked by weather forecasters. Their genesis usually takes place over warm oceans within the tropics from weak disturbances. With the right conditions, these tropical storms can gradually increase in size, strength and potentially become dangerous as they get closer to populated areas.

Major hazards commonly associated with any hurricane are storm surge (large dome of water 50 to 100 miles wide and as high as 15 feet affecting coastal areas), dangerous winds, tornadoes and torrential rains. A typical hurricane can bring at least 6 to 12 inches of rainfall where it crosses [1]. Torrential rains are particularly dangerous when a storm is moving slowly. The ground saturates very fast and depending on the area affected, destructive flooding, mudslides, and flash floods may occur. In the continental United States, damages due to such storms in 2007 averaged $10-11 billion [2]. This figure is expected to increase as population, wealth, and development on the coastline grow. It is therefore crucial to provide to the population adequate warnings, advisories, and precise weather forecasts so as to protect life and property as much as it is possible.

Hurricane forecasting cannot effectively occur without the use of technical instruments and sensors to help monitor, measure, analyze, and predict atmospheric processes such as hurricanes. Critical parameters such as rain rate, storm size, wind speed, wind direction are but a few that need to be estimated for better forecasting. These parameters can be measured using sensors mounted on buoys scattered in the ocean, as well as remote sensing instruments installed on geostationary or polar orbiting satellites. In this thesis, we are particularly interested in analyzing the performance of the scatterometer SeaWinds, which is installed on the QuikSCAT satellite platform, for tropical storm analysis. SeaWinds (commonly referred as QuikSCAT) is a scatterometer designed to infer wind speed and direction over the ocean from radar backscatter measurements. QuikSCAT wind products were originally destined to the scientific community for research purposes; however, its products have been used by the weather forecasting community throughout the world a few years after being operational in 1999. Originally designed for a three year mission, QuikSCAT is still providing wind data on a daily basis ten years after its launch.

1.1 Proposed work

The standard wind product (L2B) derived from QuikSCAT backscatter measurements provide wind data on a 25 km swath grid. This resolution of QuikSCAT data can be enhanced by implementing the AVE algorithm [3] which enables the estimation of wind data on a 2.5 km swath grid (known as Ultra-High Resolution or UHR). Visual images showing wind speed and/or direction can be created using L2B and/or UHR, and interpreted by a human. L2B images are commonly used by the Ocean Prediction Center (OPC) to issue marine warnings, forecasts, and guidance for maritime users. These images can also be used to analyze hurricanes.

In [4], performance of UHR versus standard L2B QuikSCAT images in tropical storm analysis is done. Circulation center identification is analyzed using both sets of images. Resolution enhanced images are found to provide additional storm structure. It is desired to build upon this analysis and provide a comprehensive study of QuikSCAT's effectiveness in determining two specific storm parameters, in two ocean basins (Atlantic and Eastern Pacific oceans), that is tropical storm eye center location and wind radii estimation. The former is discussed in [4]. In this thesis, a new and different approach is proposed in analyzing tropical storm eye center location to reinforce the effectiveness of using QuikSCAT UHR images in hurricane analysis. Since wind radii are another important criteria of all tropical storms, which helps determine the storm size, intensity, and potential zone of destruction, analysis of QuikSCAT performance in estimating wind radii is explored. A method to automatically estimate this metric is presented and evaluated.

1.2 Thesis outline

This thesis is divided into five chapters. Chapter 2 covers background information regarding Tropical Cyclone (TC), basics on scatterometry technology, and scatterometer Seawinds on QuikSCAT.

Chapter 3 provides a comprehensive analysis of QuikSCAT UHR images' effectiveness in identifying TC eye center location. This evaluation is done for all TC cases in the Atlantic and Eastern Pacific basins since QuikSCAT became operational (i.e. 1999) up to 2007.

In Chapter 4, TC wind radii are manually estimated and visually compared with H*wind and the Extended Best Track data sets. A data modeling technique is introduced in Chapter 5 to enable wind radii estimation in an automated fashion. Performance is measured against EBT data set.

Chapter 6 concludes this thesis by summarizing the various analyses presented, and discusses possible future work.

Chapter 2

Background

Out of all known weather disturbances, hurricanes are one of the most feared, deadly, and catastrophic. For centuries, these storms have been studied by the scientific community, and yet are still not fully understood and predictable. Since the mid-1970s observations and measurements of hurricane parameters increased, mostly due to the use of remote sensing devices and computer models [5].

This chapter defines and describes such weather disturbance and some of the instruments (particularly scatterometers) used to measure, estimate, and help forecast hurricanes. An explanation of scatterometry is also provided, as well as an extended introduction of the scatterometer SeaWinds on QuikSCAT.

2.1 Tropical Cyclones

A hurricane is an example of a more general weather phenomena called a tropical cyclone. This section defines a tropical cyclone and provides key characteristics. It also discusses the challenges U.S. weather forecasters face in predicting and tracking such storms, as well as a brief description of the instruments used to perform such tasks.

2.1.1 Key characteristics

A tropical cyclone (TC) is a natural cyclonic weather phenomena or storm which generates over warm oceans (with a temperature greater than 27°C) from pre-existing disturbances. Key characteristics of a TC include a center of low pressure usually called the eye of the storm, a closed surface wind circulation about the eye center, spiral rain bands, an eyewall where winds are usually the strongest, and organized deep convection. Figure

2.1 illustrates all these characteristics in a single diagram to help understand the basics of tropical cyclones.

The eye of the storm is usually well defined. Its diameter can vary between 30 and 65 km. Calm winds and clear sky can be associated with this region of the storm, as well as a much lower atmospheric pressure (ranging from 890 mb to a little below 1000 mb, 1013 mb being standard ambient atmospheric pressure) [6]. In contrast, right at the boundary of the eye is the eyewall where winds, accompanied with thunderstorms, are the strongest and the most dangerous. Wind circulation around the eye is counter-clockwise in the northern hemisphere and clockwise in the southern hemisphere as a result of the Coriolis effect. In the northern hemisphere, most TCs travel from the east to the west. Combined with the counter-clockwise wind circulation, winds are found to be stronger and most destructive in the east quadrants of the storms. The opposite is found in the southern hemisphere.

Spiral rain bands accompany the wind circulation around the TC and can extend a few hundred kilometers from the center. These bands of thunderstorms can range in width from a few kilometers to tens of kilometers and are 80 to 500 kilometers long [1]. Deep convection refers to the vertical heat transfer extracted from the warm ocean. This transfer of energy is the major element responsible for sustaining a TC's life or even strengthening it. This process usually is strongest around the eye of the storm.

2.1.2 TC types

TCs are ranked by their intensity, which is primarily estimated using the maximum one-minute sustained wind speed metric. This measurement is the temporal average of sample wind measurements obtained over a minute period. Maximum measurements are usually observed around the eyewalls where strongest winds are present.

There are officially three types of TCs: tropical depressions, tropical storms, and hurricanes. Furthermore, there are five categories of hurricanes defined according to the Saffir-Simpson hurricane scale which is used to measure the storm's structural effects [5]. A listing of these various TC types and hurricane categories can be found in Table 2.1.

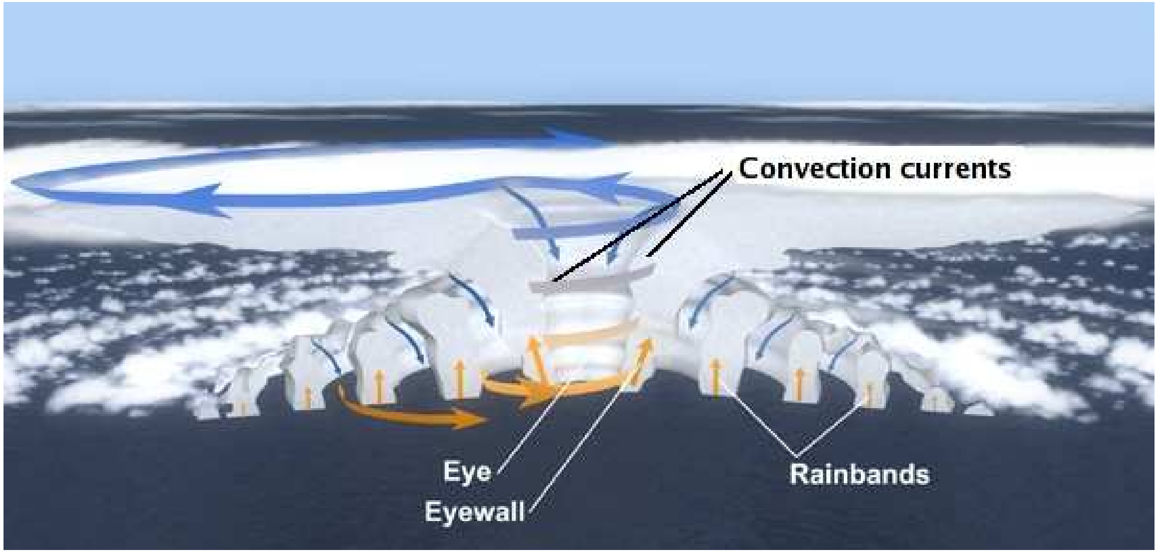

Figure 2.1: Diagram showing key characteristics of a typical mature tropical cyclone. These key characteristics include a center of low pressure (the eye), the eyewall, spiral rain bands which accompany the wind circulation, and the convection currents where heat is extracted from the warm ocean and transfered vertically [7].

Table 2.1: Tropical Cyclone Types and Hurricane Categories according to the Saffir-Simpson Hurricane Scale

TC type	Wind Speeds (1-min max sustained)
Tropical Depression	less than 63 km/hr
Tropical Storm	64-118 km/hr
Hurricane Cat 1	119-153 km/hr
Hurricane Cat 2	154-177 km/hr
Hurricane Cat 3	178-209 km/hr
Hurricane Cat 4	210-249 km/hr
Hurricane Cat 5	greater than 249 km/hr

It is interesting to note that if a TC falls into the hurricane category, it is called a hurricane in the Atlantic and Eastern Pacific basins, a Typhoon in the Western Pacific basin, and a Cyclone in the South Hemisphere, Indian Ocean and South Pacific basins.

2.1.3 Tropical Cyclone forecasting in the U.S.

In the United States of America, the National Hurricane Center (NHC) located in Florida and the Joint Typhoon Warning Center (JTWC) located in Hawaii are the two major hurricane weather centers. They have been operational since, respectively, 1955 and 1959. These specialized weather centers are responsible for tracking tropical cyclones and providing accurate forecasts and appropriate warnings to populations who may be affected by such storms. NHC is responsible for issuing TC warnings for the Atlantic and Eastern Pacific oceans, while JTWC issues them for the North West Pacific Ocean, South Pacific Ocean and Indian Ocean.

Despite the advances in weather forecasting technology throughout the years, tracking and forecasting TCs are still very complex and challenging tasks. There are 4 major classes of sensors currently used to estimate TC characteristics: buoys, ships, specially designed aircraft, and remote sensing instruments on satellites. Since much of the desired data acquisition is at sea level, buoys and ships are good ways to obtain accurate TC key measurements. However, the major problem is resolution: for practical reasons, there are only a certain number of buoys at sea, thus hindering measurement resolution. And though most commercial ships are equipped with various weather measuring devices, they naturally adjust their routes so as to avoid direct contact with TCs. As a result, they generally do not provide direct measurements of major TC characteristics.

Specially designed aircraft are used by the NHC to fly through TCs and retrieve wind, pressure, convection measurements and other TC parameters. One major problem with this technique is that it requires the weather disturbance to be within flying distance of the coast. Moreover, resolution is still an issue since some TCs can be very large and thus difficult for a single aircraft to provide adequate measurements over the area covered by the storm.

2.1.4 Use of remote sensing instruments in TC forecasting

Remote sensing instruments installed on satellites are tools to monitor TCs out of range of coastal radars (more than 270 km / 150 nmi) [8]. There are various types of remote sensing instruments, each designed with a specific purpose. The most common sensors for TCs are found on geostationary satellites. The Geostationary Operational Environmental Satellite (GOES) program is a key element of the U.S. weather services [9]. There are currently two operational sensors, namely GOES-11 and GOES-12 which provide data in near-real time to weather forecasters. These instruments provide optical and infrared imagery as well as atmospheric sounding, which are made available several times per day. With such measurements, it is possible to infer the eye location of a storm, its size, and possibly its track. However, these sensors have some major limitations since they do not provide information of the wind conditions underneath the storms and may not be able to help infer eye location if the latter is covered by cloud.

On the other hand, low Earth-orbiting satellites can help infer these critical storm characteristics as well as early detection of tropical depressions [10]. These satellites carry either active or passive sensors, or both. Each sensor type is designed to help determine particular storm information. For example, NHC and JTWC currently use the AMSU sensor to measure temperature and moisture soundings to eventually estimate the storm warm core; the Special Sensor Microwave/Imager (SSM/I) is another passive instrument which measures surface/atmospheric microwave brightness temperature to help estimate near-surface wind speed, total columnar water vapor, and total columnar cloud liquid, precipitation. SeaWinds on QuikSCAT (commonly referred as QuikSCAT) is also used specifically to estimate near-surface wind speed and direction. All these remote sensing devices are indispensable in helping understand, and estimate TC characteristics.

2.2 Scatterometry technology and SeaWinds

Since QuikSCAT is of particular interest in this thesis, this section provides a description of scatterometry technology, the key features of this sensor, and the products obtained from QuikSCAT to help infer wind fields over the ocean.

2.2.1 Basic principles of scatterometry

Scatterometry is a form of remote sensing which specifically focuses on measuring geophysical properties of the surfaces or volumes targeted. A scatterometer is a device designed both to send microwave pulses from an antenna towards a target, and to receive and measure backscatter power P_r from it. This latter quantity can be determined using the radar equation as follows:

$$P_r = (\frac{P_t G_t}{4\pi R^2}) \cdot \sigma^o \cdot (\frac{A_r}{4\pi R^2}), \tag{2.1}$$

where P_t is the transmitted power, G_t is the gain of the transmitting antenna in the target's direction, R is the range between the antenna and the target, σ^o is the normalized radar cross-section, and A_r is the effective aperture of the antenna. It is noteworthy to mention that Equation 2.1 is used for monostatic radar where the antenna is both transmitting and receiving. Furthermore, arranging Equation 2.1 as shown explicitly shows the total amount of transmitted power (first term in parentheses), and the amount of energy the target scatters back to the antenna (last term in parentheses). The radar cross-section σ^o in this equation is of most interest and is a function of the direction of the incident wave and the wave toward the receiver. Its value is also dependent on the scatterer shape or roughness, and its dielectric properties [11]. If the target is perfectly smooth, the receiving antenna receives little signal. For instance, backscatter signal from the ocean surface can be intercepted when this latter is roughened by the wind blowing over it, which in turn generates centimeter-scale capillary waves called cat's paws. Roughness is therefore an important criteria which contributes to the intensity of backscatter signals.

In order to estimate wind speed and direction fields over the ocean, a relationship between σ^o and these geophysical quantities is necessary. This relationship is known as the geophysical model function (GMF). The GMF is based mostly on empirical models which relate ocean radar cross section and the near surface wind. It can be written as follows:

$$\sigma^o = g(|S|, \chi, ...; \theta, f, pol), \tag{2.2}$$

where $|S|$ is wind speed, χ is the azimuth angle between the incident radiation and the wind vector, ... represents the effects of non-wind variables, θ is the incidence angle measured in the vertical plane, f and *pol* are, respectively, the frequency and polarization of the incident wave [12].

Even with a known GMF, a single σ^o measurement over a given resolution cell is not sufficient to determine wind speed and direction. For each given σ^o, the GMF is inverted and yields multiple solutions for the wind fields; for a fixed wind speed and σ^o value, more than one azimuth angle solutions are possible (see Fig. 2.2). It is therefore necessary to obtain multiple σ^o measurements from various azimuth angles over a given resolution cell.

More accurate wind speed results are thus achievable, though multiple solutions (ambiguous vectors) are still possible for the wind direction. Additional processes are required to decide which ambiguity to choose.

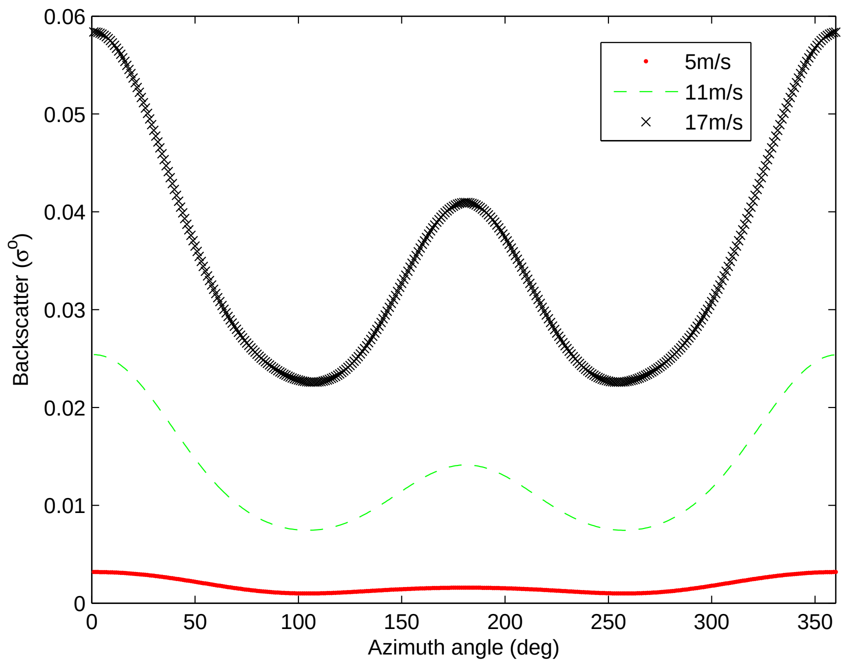

Figure 2.2: Plot of the backscatter signal versus azimuth angle for three fixed wind speeds. As shown on this plot, more than one azimuth angle value are associated to a single σ^o measurement given a fixed wind speed.

2.2.2 Scatterometer Seawinds on QuikSCAT

Seawinds on QuikSCAT satellite was launched on 19 June 1999 and is still operational as of 7 July 1999. It is the first wind-vector scatterometer using a dual scanning pencil-beam rotating antenna. QuikSCAT operates at a single Ku-band frequency of 13.4 GHz and flies on a sun-synchronous polar orbit 803 km above the earth. This sensor has been designed to measure the normalized radar backscatter (σ^o) at 25 km resolution over the ocean. σ^o measurements are collected over a 1800 km wide swath at two nominal incidence angles, 46^o (h-pol) and 54.1^o (v-pol) as shown in Fig. 2.3. Such configuration improves Seawinds wind direction determination, particularly in mid-swath (about 200-700 km on either side of the satellite track) as four types or "flavors" of σ^o measurements are possible: inner-forward, outer-forward, inner-aft, and outer-aft (see Fig. 2.3). However in the far swath (between 700 and 900 km on either side of the satellite track), only two flavors of σ^o are available, thus reducing quality in wind retrieval in this area [13].

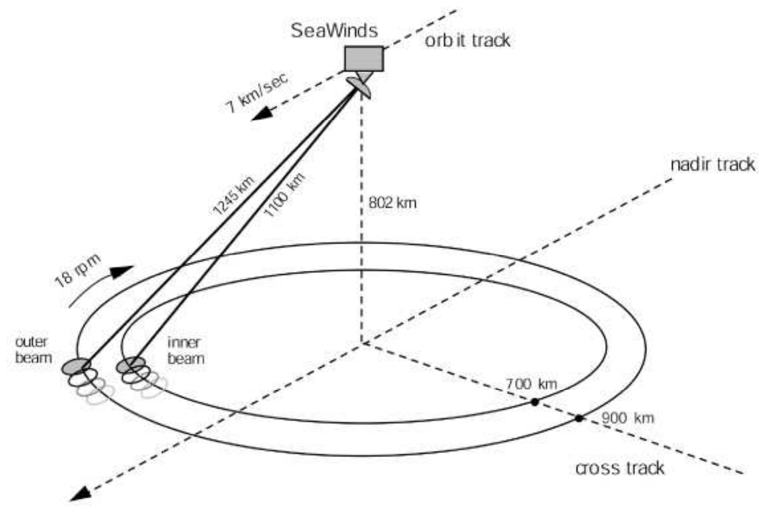

Figure 2.3: SeaWinds viewing geometry (image courtesy of [14]).

Since QuikSCAT travels at about 7 km/s, each orbit is about 101 min long which results in approximately 14 revolutions (revs) per day. Combining its 1800 km wide swath with the number of daily revs, QuikSCAT is capable of measuring σ^o for about 90% of the ice-free ocean in 24 hours. σ^o measurements are made available in near-real time. Data gaps are exceptionally low; for example, about 98.8% of the total time between rev 430 (July 1999) and rev 23970 (January 2004) QuikSCAT has succesfully collected data [13].

2.2.3 QuikSCAT standard L2B product vs. Ultra High Resolution

When raw telemetry data from QuikSCAT is processed and analyzed, it is then made available near-real time to the scientific community for distribution as various geophysical data products. These products are organized in different levels (level 1B through level 2B).

Level 2B (L2B) data product lists the ocean wind vectors in 25 km swath grid [15]. This product is of most interest and is mostly referred as QuikSCAT standard L2B product.

Such product is commonly used by various weather and research centers throughout the world. For example, the Marine Prediction Center (now called Ocean Prediction Center) forecasters have been using this data extensively since July 2001 to help ensure the safety of ocean-crossing commercial ships and other type of vessels traveling on the high seas [16]. Hurricane forecasters are also using QuikSCAT data since hurricane season 2000-2001 to help identify TC characteristics and help in early detection of tropical depressions.

With standard L2B product, decent images of hurricanes can be obtained simply by plotting the wind vectors straight from the L2B product (see Fig. 2.4(a)). Though a few structural features in TCs are somewhat identifiable in this figure (such as the eye center, eyewalls and storm size), ambiguity selection errors and low resolution can hinder the ability to distinguish such features. The AVE algorithm [3] can be used to enhance backscatter resolution which can ease TC feature identifications. This algorithm takes advantage of the multiple spatial and temporal overlap of σ^o slice values to eventually enhance the resolution. The final product obtained from this technique is called Ultra High Resolution (UHR) product in 2.5 km swath grid. This product is made available through the National Environmental Satellite, Data, and Information Service (NESDIS) "manati" Web site (http://manati.orbit.nesdis.noaa.gov/quikscat/). For comparison, L2B and UHR images are provided for a given TC case in Fig. 2.4. Although much more prone to noise and rain contamination, UHR images provide more details in the wind speed field compared to L2B images as shown in Fig. 2.4.

2.3 TC characteristics used in QuikSCAT UHR wind product validation process

In this thesis, two key structural features in TCs, such as eye location and wind radii, are selected and used as means of showing the value of using QuikSCAT UHR wind product in TC analysis and forecasting. Details about these features are provided in this section so as to justify their choice in helping to validate QuikSCAT UHR wind product.

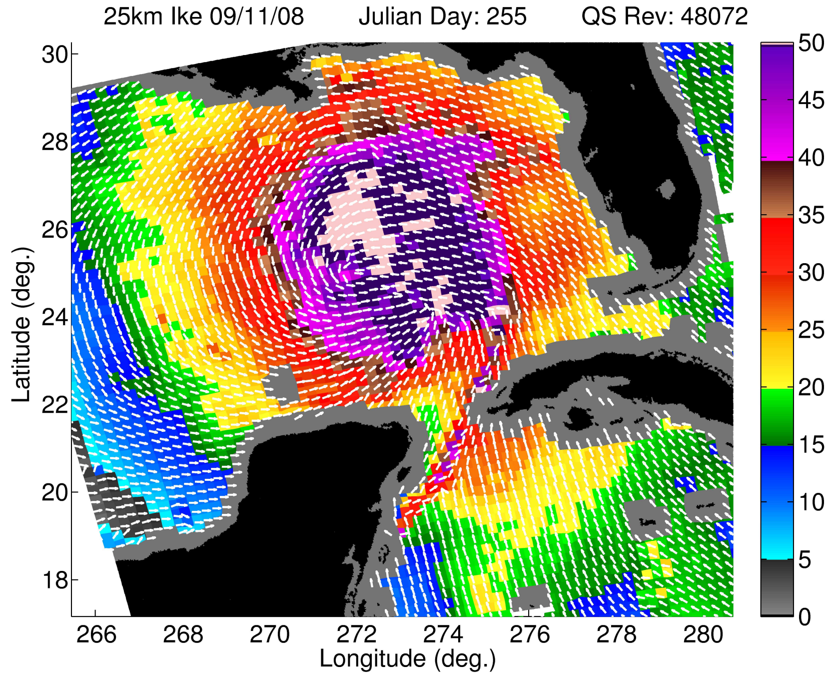

(a) An example of a standard resolution (L2B) image.

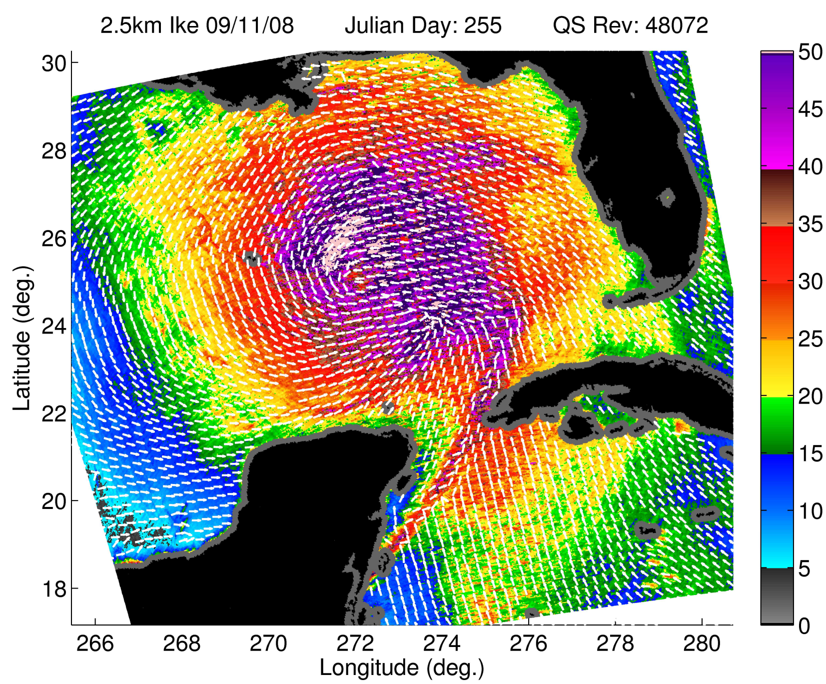

(b) An example of an ultra high resolution (UHR) image.

Figure 2.4: TC Ike in the Gulf of Mexico (1136 UTC 11 Sep. 08) shown here in both standard (a) and enhanced (b) resolutions. Note the additional details provided with the UHR image such as a well defined eye center, eye wall and overall refined wind speed field. Color scale is in knots.

2.3.1 TC eye center location

Eye center location is a very important TC feature which is reported during TC tracking and forecasting. Very strong winds can be found around the eye circumference (eyewalls). Knowing the eye location and its relative size is critical in helping forecast TC motion intensity. As mentioned earlier, standard L2B product can help determine TC location though it can be very difficult at times. It is therefore of interest to demonstrate whether UHR product can be more effective in identifying TC eye center locations.

Best-track data is the only resource available which provides accurate TC eye locations. As a result, this dataset is used as ground truth for this analysis. Best-track data is provided by NHC for the Atlantic and Eastern Pacific basins. For each named TC, it provides the eye location, maximum sustained wind speed and atmospheric pressure at the eye center every six hours over the storm lifetime. This dataset is usually available several months after a given hurricane season; several different types of post-analysis are required to confirm and set the best possible storm track dataset. Best-track data should then be the best choice to use as ground truth to help validate QuikSCAT UHR TC eye locations. The results of this validation process are provided in chapter 3.

2.3.2 Wind radii

Wind radii is another important metric which can be used to demonstrate QuikSCAT UHR wind product advantages in its use in TC analysis. As part of the National Weather Tropical Cyclone Forecast Advisory products, NHC is required to report the maximum wind radius in each quadrant of a given storm, at three different wind speeds (34kt, 50kt, and 64kt). Estimating wind radii for each TC tracked by NHC is critical since this metric can help determine the possible extent of storm surge, dangerous waves, wind patterns, etc. This in turn helps in readjusting shipping routes if necessary, and helps provide a better estimate of the storm size, which can help the NHC know how much of the coastal population needs to be warned and/or evacuated.

Wind radii are usually estimated by combining measurements from jet aircraft flying over the storms, from buoys, and microwave remote sensing devices. This metric is particularly difficult to estimate when jet aircraft data is not available; since TCs spend most of their lifetime far from the coast, jet aircrafts cannot reach them and therefore wind radii estimates depend exclusively on sparse buoys measurements and microwave remote sensing devices. Chapter 4 covers in great detail the procedure used to achieve this task and also includes results.

Chapter 3

QuikSCAT UHR wind product validation based on TC eye location

The purpose of this chapter is to evaluate the effectiveness of Seawinds on QuikSCAT in helping identify TC eye locations. The first section briefly describes image rendering, compares ultra high resolution images versus standard resolution images and introduces a “confidence” flag. The next two sections provide a detailed data analysis for the year 2006 and summary results for the years 1999 through 2007. Finally in the last section, the reliability of QuikSCAT wind products for TCs analysis is discussed by evaluating how often useful data is received daily.

3.1 Eye center identification method

3.1.1 Image rendering

Standard wind product (L2B) available operationally in near-real time are constantly retrieved from SeaWinds on QuikSCAT at 25 km resolution. An ultra high resolution (UHR) product is also created for each named TC. For comparison, we use best-track data from the National Hurricane Center (NHC) as well as the Joint Typhoon Warning Center (JTWC) for the five major ocean basins (Atlantic, Indian Ocean, South Hemisphere, Western and Eastern Pacific). The data is used to co-locate QuikSCAT passes with TC eye locations. Since best-track data provides eye location only every six hours for a given TC, a QuikSCAT pass over any TC rarely matches best-track time. To solve this problem, we use a parametric spline interpolation technique to approximate the best-track eye location corresponding to the time of each QuikSCAT pass over a TC.

Two sets of gif images are eventually created at different resolutions for each given TC pass within a basin. The first set of images (L2B) contains wind direction and speed fields with a standard resolution of 25 km, whereas the second set (UHR) has an ultra high resolution of 2.5 km. Each image is manually analyzed to locate the eye center of the TC. Ultimately in this image analysis, our purpose is to compare the error distance between our manual eye center location to best-track's in order to evaluate QuikSCAT's effectiveness in TC analysis.

3.1.2 Confidence level with UHR images

With L2B wind product the storm pattern can be recognized. However, ambiguity selection errors and low resolution can limit the analyst's ability to identify particular TC characteristics such as eye center, eye walls, and other key features. The resolution improvement [3] from a 25 km grid to a 2.5 km grid resolution enables the analyst to identify TC characteristics much faster and easier. Although much more prone to noise and rain contamination [17], UHR images provide more detail in the wind speed field compared to L2B images.

Since we have subjectively more confidence in identifying the eye location at higher resolution, UHR image analysis is divided into two categories depending on the confidence level of identifying the eye in each image. The first category includes images in which we have high confidence in the eye center location; the second category includes images where eye center identification is possible but with a low to medium level of confidence. In general, the latter category includes images of incipient systems, TCs with equivocal wind patterns, TCs half way over land or cropped images which only partially cover a TC. The top plot of Fig. 3.1 is a good example of an incipient system. This UHR image would be considered low confidence because it is difficult to decide where the eye of the TC is or if it exists. On the other hand, the bottom plot of Fig. 3.1 is a good representation of what we would consider as a high confidence case. In this figure, the eye is identifiable unambiguously. One can argue that these confidence levels are defined subjectively since the analyst is the one judging whether the eye location is of low or high confidence. Nonetheless, separating the images into these two categories may be a good way to evaluate QuikSCAT effectiveness in helping identify TC's eye locations.

In each confidence category, a table with the standard deviation, mean, and median of the error distance (in kilometers) between our eye center location visually identified and

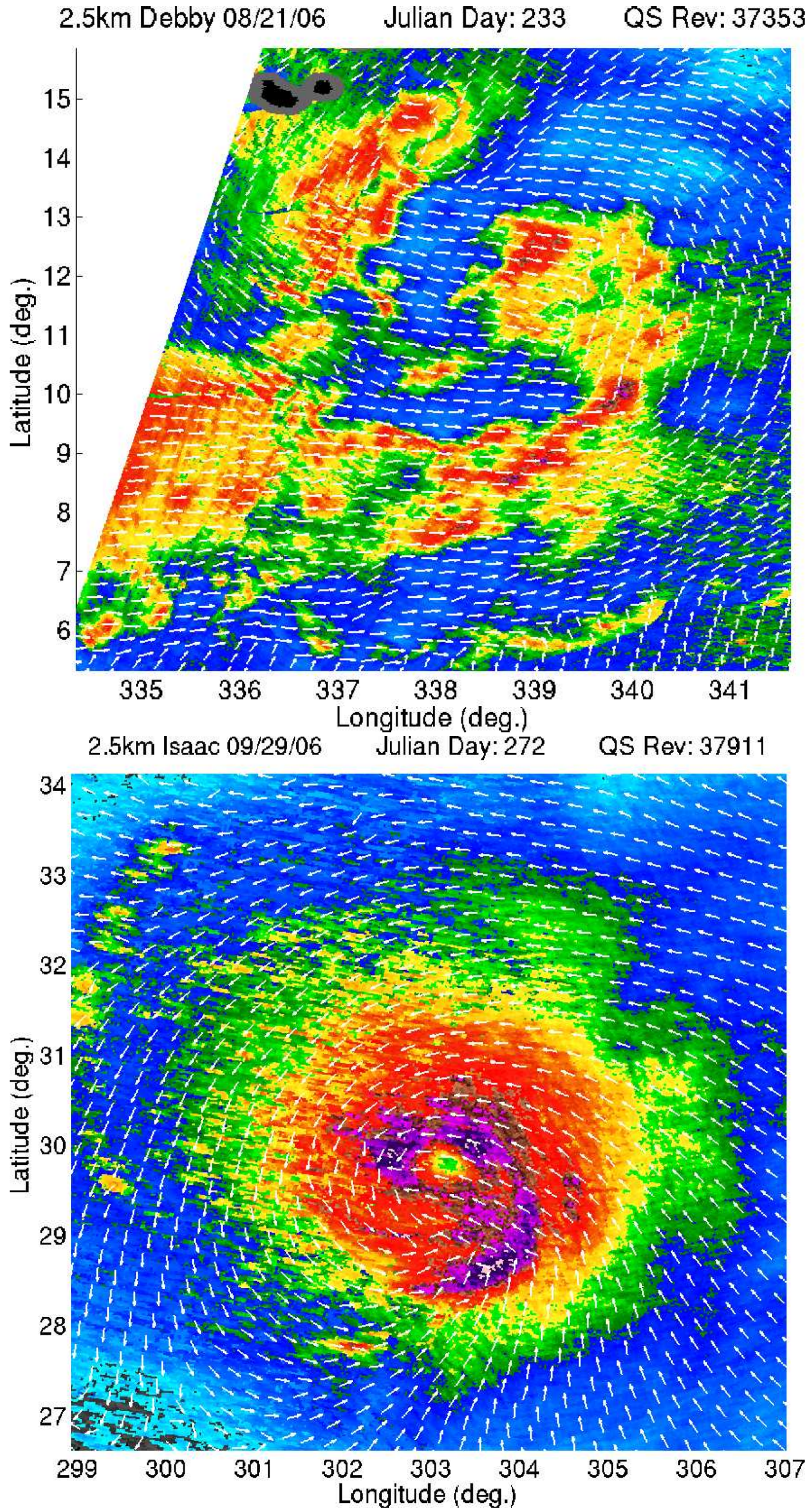

Figure 3.1: Two UHR wind field images showing TC Debby (top image considered as low confidence) and TC Isaac (bottom image considered as high confidence) in the Atlantic Ocean in 2006. In the low confidence image, the eye location (if it exists) is clearly difficult to identify accurately. Whereas for TC Isaac, the eye location is unambiguous thanks to the detailed UHR wind speed field.

the interpolated best-track eye location is created. For each basin studied, histograms based on these error distances are plotted and analyzed.

3.2 Results for the year 2006

A detailed analysis of the year 2006 in the Atlantic and Eastern Pacific basins is provided in this section to illustrate the results obtained for a given hurricane season.

3.2.1 The Atlantic basin

In 2006, 10 named TCs swept through the Atlantic (ATL) basin. For these 10 TCs, 112 UHR and 98 L2B images from SeaWinds on QuikSCAT were analyzed for this particular basin. An error distance histogram is plotted for each set of images (see Fig. 3.2). The error distance represented in this figure is between the interpolated best-track eye location and the analyst's. By comparing both histograms, we can notice a 20 % improvement in the mean

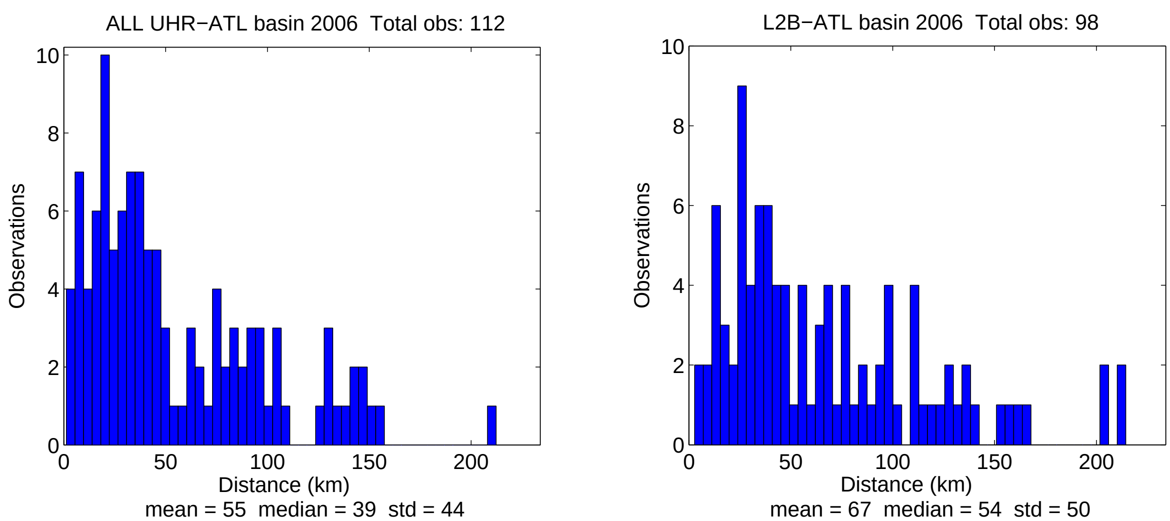

Figure 3.2: Error Distance between interpolated best-track eye location and analyst's for all TCs in the ATL basin in 2006 (left plot: UHR; right plot: L2B). There is a 20 % improvement in the mean error using UHR images over standard L2B.

error using UHR images over standard resolution images as well as a slight improvement in the median and standard deviation. Yet, close analysis of Fig. 3.2 indicates that the error between the analyst and the interpolated best-track eye location is still significant for a moderately high number of UHR images. This results in a somewhat high mean error of 54 km and may not be convincing enough to show the effectiveness of UHR images in identifying a TC's eye. Consequently, the statistics are further analyzed and split into the two confidence categories described in subsection 3.1.2.

Low confidence category

An analyst concluded that 77 out of the 112 UHR images for the ATL basin fall in the low confidence category. A histogram of error distances for these low confidence images is shown in Fig. 3.3 (left plot). For this category, the mean error distance is 67 km (20 %

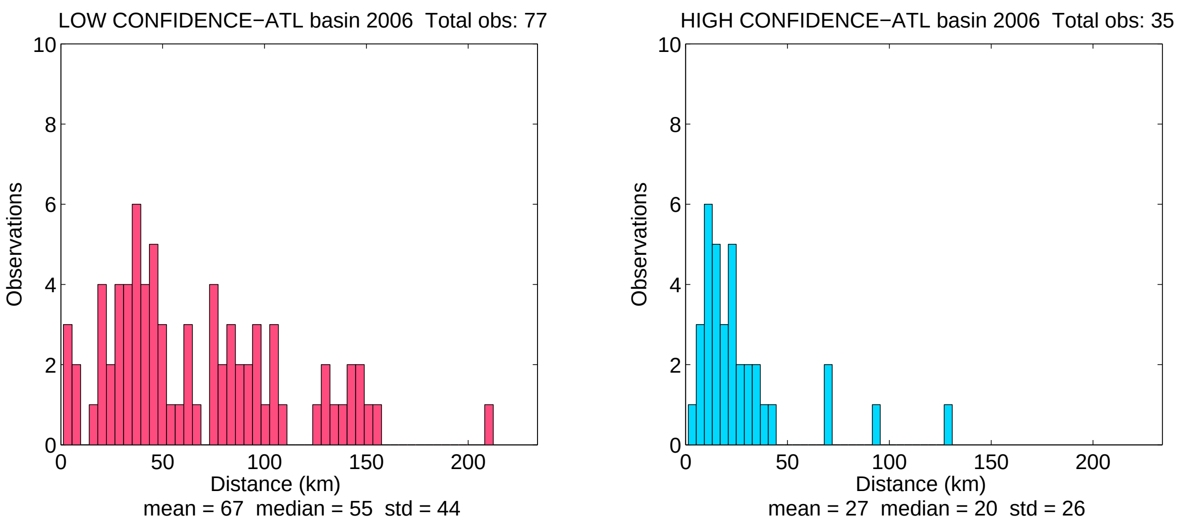

Figure 3.3: Error Distance between interpolated best-track eye location and analyst's for the ATL basin in 2006 (left and right plots, low and high confidence UHR images respectively). High confidence UHR images result in a much lower mean compared to low confidence images. A closer look to the high confidence error plot indicates three cases with surprisingly large error distance.

higher than the mean error for all UHR images combined), with a median of 55 km and a standard deviation of 44 km. Despite the low confidence criteria given to these images, a non-negligible number of them have an error distance below 50 km (37 out of 77). Thus, even if the analyst is not sure where the eye location of a TC is, reasonable results can be obtained for the eye location.

High confidence category

A total of 35 observations in the ATL basin were considered of high confidence. In this case, the mean error distance to the interpolated best-track eye location is 27 km; the median and standard deviation are respectively 20 km and 26 km (see right plot of Fig. 3.3). Table 3.1 regroups these statistics along with those from the low confidence category and all UHR images combined. The mean error distance obtained from the high confidence set of

Table 3.1: Statistical results for UHR images for the ATL basin in 2006

	Mean error(km)	Median(km)	Stand. dev.(km)
All UHR	55	39	44
Low Confidence	67	55	44
High Confidence	27	20	26

observations shows a noticeable improvement from not only the low confidence but also the overall set of UHR observations. From 55 km (all UHR images combined), the mean error decreases to 27 km which is a 51 % improvement. Typically, hurricane eyewalls of developed TCs have a diameter of 20 to 60 km [6]. The 27 km mean error for the high confidence set of observations means that on average the analyst can easily pinpoint the eye center of a TC. By taking into account the 26 km standard deviation, the analyst can find the eye center of a TC in almost every single high confidence UHR image.

Even with such good results obtained from the high confidence category, it is interesting to note that 4 observations have an error distance greater than 60 km (see right plot of Fig. 3.3); these errors range from 68 km to 131 km. Such large errors are surprising. Further analysis of these observations led us to the conclusion that there is an error in the best-track data. By neglecting these 4 unusual error distances greater than 60 km, the mean error distance for the high confidence category decreases from 27 km to approximately 19 km (a 65 % improvement compared to all UHR images combined); the median decreases from 20 km to 18 km and the standard deviation from 26 km to 10 km. For this particular basin, high confidence UHR images represent 31 % of all UHR images analyzed. The same analysis is then performed on TCs in the Eastern Pacific basin for the same year to check if similar or better results are achieved.

3.2.2 The Eastern Pacific basin

The Eastern Pacific (EP) basin hosted a few more TCs than the ATL in 2006. In fact, 19 named TCs are recorded for that year as opposed to 10 for the ATL. In the EP basin, 160 UHR images from SeaWinds were analyzed. As with the ATL basin, images were subjectively classified low or high confidence.

Low confidence category

A total of 84 out of the 161 observations are considered low confidence. The error distribution for these observations is shown in Fig. 3.4 (see left plot). It is interesting to

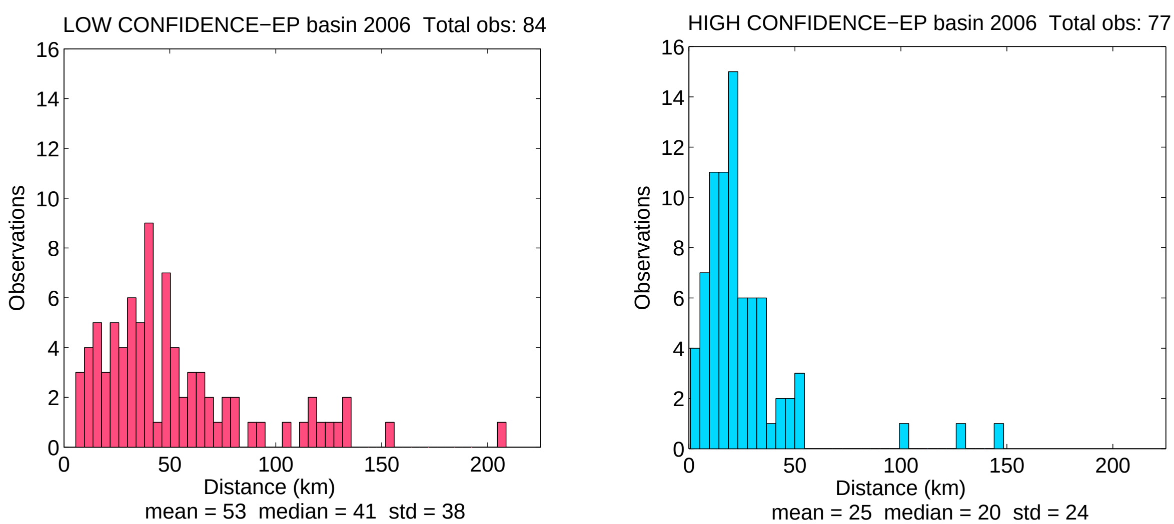

Figure 3.4: Error Distance between interpolated best-track eye location and analyst's. Once more, high confidence UHR images result in a significantly lower mean error compared to the low confidence images.

note that most of the low confidence observations have an error distance below 50 km. The mean error is 53 km with a 38 km standard deviation and a 41 km median. Even with more observations than the ATL basin, the low confidence category for the EP basin has smaller mean and standard deviation. Such outcomes support the conclusion drawn with the low confidence images for the ATL basin: it is still possible to obtain results close to the interpolated eye location with low confidence images.

High confidence category

In the Eastern Pacific basin 77 UHR images out of 161 are considered high confidence, which is almost half of all the analyzed UHR images for this basin. The right plot of Fig. 3.4 shows the error distribution. The mean error improves 53 % (25 km compared to 53 km) from the low confidence set of images. The standard deviation is 24 km and the median 20 km. Up to 95 % of these observations have an error below 50 km. Even so, 3 observations yielded unusual error distances (between 100 and 150 km). Further analysis of these images lead us to the same conclusion as for the ATL basin: best-track data was misleading in these rare cases. By omitting these 3 unusual error distances, the mean error for the high confidence category improves by 16 % and goes down to 21 km. This result is consistent with the one obtained for the ATL basin (19 km mean) and supports the conclusion in Section 3.2.1 pertaining to the effectiveness of QuikSCAT images in identifying TC's eye locations. This same statistical analysis is now applied to all TCs in the Atlantic and Eastern Pacific basin from the beginning of QuikSCAT operation to the year 2007.

3.3 Results for the years 1999 to 2007

Since the launch of QuikSCAT (19 June 1999) up through 2007, a total of 1719 relevant UHR images from SeaWinds have been generated for TC analysis in the ATL and EP basins. Additionally, SeaWinds on ADEOS II (launched 14 December 2002, failed 24 October 2003) provided another 193 relevant UHR images for the year 2003. The confidence flag is used to categorize the images and yearly error distance results are derived and compared for each basin.

3.3.1 High and low confidence categories for the ATL basin

For the ATL basin, the low and high confidence categories encompass, respectively, 424 and 601 UHR images. Table 3.2 shows the statistical results (mean error distance, standard deviation, median as well as the number of low/high confidence observations) for the years 1999 through 2007. The corresponding error plots of the yearly means with their

Table 3.2: Statistical results for low/high confidence UHR images in the ATL basin for the period 1999-2007. The table provides yearly mean, median and standard deviation (in kilometers) for each confidence category for the difference between analyst manual eye locations and interpolated best-track eye locations.

ATL basin	1999	2000	2001	2002	2003	2004	2005	2006	2007
LC Mean (km)	70	61	60	57	52	70	50	67	49
LC Med. (km)	44	52	38	42	40	54	53	55	45
LC Stdv. (km)	69	53	64	54	53	70	36	44	36
Total LC obs.	38	31	43	27	84	31	44	77	48
HC Mean (km)	18	24	25	24	21	19	23	19	24
HC Med. (km)	13	21	23	19	16	15	21	18	18
HC Stdv. (km)	15	19	15	17	14	16	15	10	17
Total HC obs.	42	60	55	42	154	76	115	31	25

respective standard deviation can be found in Fig. 3.5. The curve with lower means (around 20-25 km) correspond to the high confidence category while the others with larger means to the low-confidence category. The high confidence error plot shows a fairly small and consistent average in the error distance of the TC's eye position which in turn reinforces the reliability of QuikSCAT data. For the low confidence set of images, the mean is between 50 km and 80 km while the high confidence mean is between 18 km and 25 km. It is important to note that a few observations have been identified with very large error distances similar to those found in the ATL and Eastern Pacific basins in 2006. In fact, a total of 8 different cases (spread out in the years 2000, 2001 and 2004) have such error distances. These cases have been excluded from Fig. 3.5.

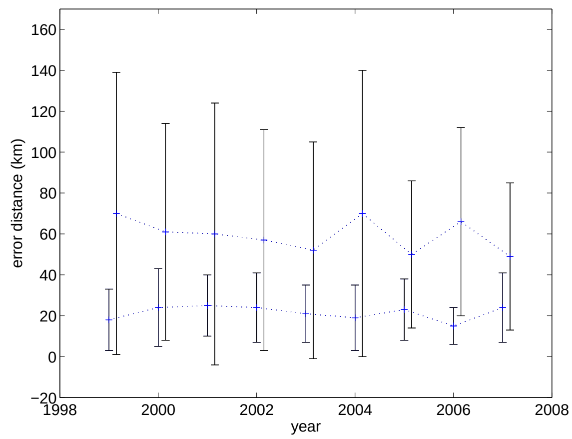

Figure 3.5: Yearly mean error plots for the UHR images in the ATL basin from 1999 to 2007. The curve with large standard deviations and yearly means greater than 60 km corresponds to the low confidence category; the other with lower yearly means and standard deviations corresponds to the high confidence category.

It is appropriate to assume from the high confidence results that the analyst is able to identify most (if not all) eye center locations of all TCs (within the high confidence category) in the ATL basin between 1999 and 2007. Since 601 out of 1025 UHR images are part of the high confidence category, eye center locations are accurately determined for about 59 % of all UHR images in this basin.

3.3.2 High and low confidence categories for the EP basin

UHR images obtained from SeaWinds provide very similar results for the EP basin though with fewer images. The low and high confidence categories contain, respectively, 363 and 524 relevant UHR images (versus 424 and 601 for the ATL basin). Statistical results for these categories are found in Table 3.3 and the corresponding error plot in Fig. 3.6. The results for the EP basin are quite similar to the ATL, except that the yearly mean and the standard deviation for the low-confidence category are on average lower. As for the high confidence category, we obtain very consistent results with a yearly mean around 24 km. This means that the analyst is able to find the TC eye location in almost all high confidence UHR images for this particular basin. This is very promising and helps demonstrate the

Table 3.3: Statistical results for low/high confidence UHR images in EP basin for the period 1999-2007. The table provides yearly mean, median and standard deviation (in kilometers) for each confidence category for the difference between analyst manual eye locations and interpolated best-track eye locations.

EP basin	1999	2000	2001	2002	2003	2004	2005	2006	2007
LC Mean (km)	40	43	67	52	54	71	48	50	42
LC Med. (km)	28	38	51	52	50	62	43	41	35
LC Stdv. (km)	35	23	51	31	32	46	38	38	26
Total LC obs.	13	26	31	25	91	36	25	84	32
HC Mean (km)	25	27	26	25	24	23	25	21	24
HC Med. (km)	21	24	21	24	20	21	20	16	20
HC Stdv. (km)	17	20	15	12	14	14	20	22	14
Total HC obs.	35	59	52	49	80	59	72	77	41

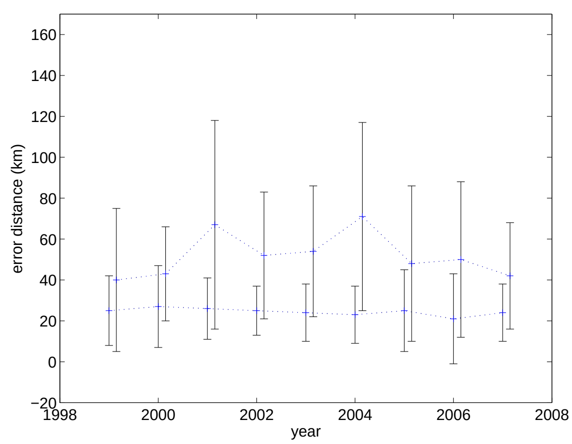

Figure 3.6: Yearly mean error plot for the low/high confidence UHR images for the Eastern Pacific basin from 1999 to 2007. The curve with higher yearly means and standard deviations corresponds to the low confidence category; the other curve with lower means and standard deviations to the high confidence category. These results are quite similar to those obtained for the ATL basin (see Fig. 3.5).

effectiveness and reliability of QuikSCAT UHR images to help find TC eye location simply by relying on the wind speed field.

3.4 QuikSCAT TC observation reliability

A key question for QuikSCAT data utility is how often SeaWinds wind products are available for cyclone tracking. The QuikSCAT satellite is in a polar orbit and revolves around the globe in approximately 101 minutes. With an 1800 km swath, it is capable of measuring the normalized radar backscatter from 90 % of the ocean twice in 24 hours. In the areas where most TCs occur, at most two observations per day are available (see Fig 3.7; in some rare locations such as the Gulf of Mexico, up to three times. Thus, when tracking a TC it may be possible to obtain two UHR images from QuikSCAT daily. However, eye locations may not always be identifiable in every image; at times TCs may be only partially covered, part-way over land, or incipient. Such images may not be useful for TC analysis.

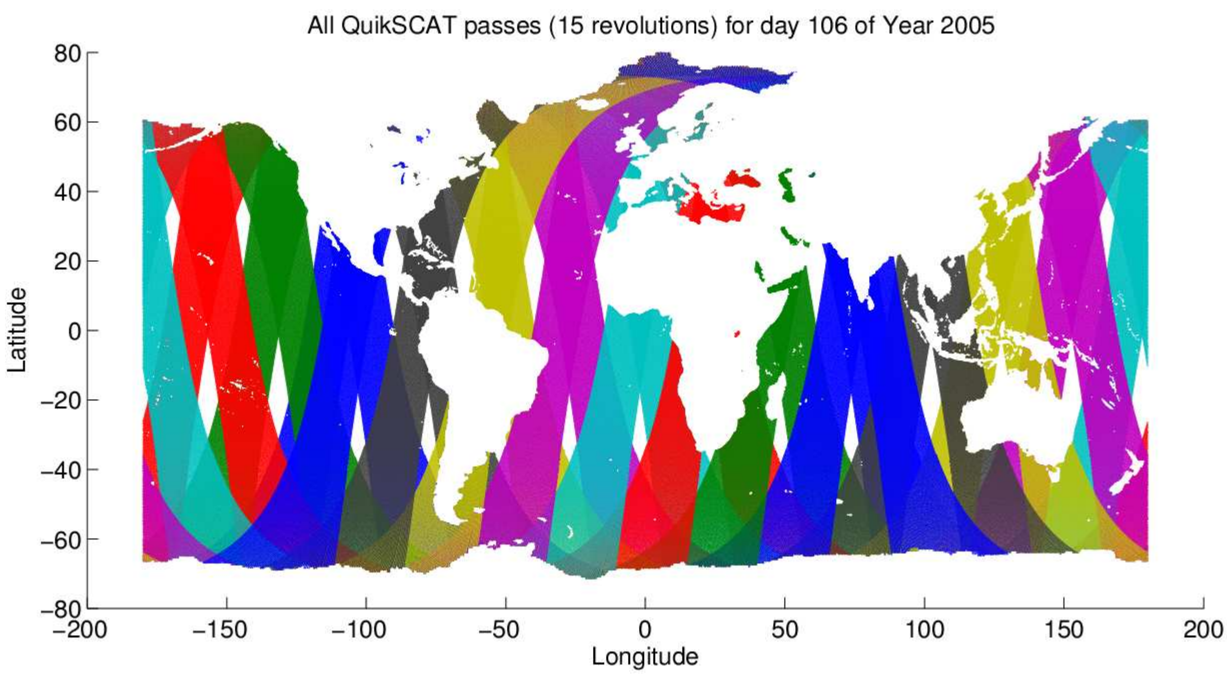

Figure 3.7: QuikSCAT daily passes (about 15) overlaid on world map for day 106 of year 2005. A color is associated to each pass.

Our purpose is to evaluate how often QuikSCAT UHR images could have been useful since the beginning of its operation. The analysis is done on a storm-by-storm basis. For each TC, UHR images are placed under two main categories depending on the number of

QuikSCAT images received per day. Once they are placed in these categories, the usefulness criteria come into play; the images are either considered useful or not. Figure 3.8 illustrates the results of this analysis for the ATL basin using bar graphs. Due to the complex nature of this figure, two examples are provided below to show how to effectively interpret it. First we desire to analyze in the ATL basin TC Olga in 2001 (TC number 15—see third bar graph in Fig. 3.8). As indicated on the plot, the TC life is 12 days. 10 out of these 12 days, two co-located images per day are obtained for TC analysis (as shown in the top portion of that plot). Out of these 10 days, 50 % of the time both images are considered useful to the analyst; 40 % of the time, only one is considered useful and 10 % of the time none of them are. The bottom portion of the plot show cases where only one co-located QuikSCAT image is obtained in a day. For TC 15, it occurred twice. Only once out of these two days, the obtained image is found to be useful for TC analysis. Overall, at least one useful QuikSCAT UHR image per day is available 83 % of Olga's TC life, while two useful UHR images per day is available 42 % of it. For the second example, we choose TC Noel in 2007 (TC number 14—see ninth bar graph in Fig. 3.8). As indicated on the plot, the TC life is 13 days. 8 out of these 13 days, two co-located images per day are obtained for TC analysis (as shown in the top portion of that plot). Out of these 8 days, 50 % of the time both images are considered useful to the analyst; 25 % of the time, only one is considered useful and 25 % of the time none of them are. The bottom portion of the plot shows cases where only one co-located QuikSCAT image is obtained in a day. 3 out of the 13 days when the TC was active, a single co-located QuikSCAT image was obtained daily. Unfortunately as the bar graph shows, none of these 3 images was useful to the analyst for TC analysis. Note that for 2 days, no QuikSCAT image was obtained at all for this TC (i.e. 8 days with 2 daily images; 3 days with only 1 daily image; 2 days with no images—8+3+2=13). The same analysis can be done on a storm-by-storm basis using these bar graphs in Fig. 3.8. It is then possible to appreciate how often, out of the lifetime of a given TC, useful co-located QuikSCAT images are obtained.

For more general results, pie charts are provided for each basin (see Fig. 3.9), which combine all the results obtained from 1999 to 2007. They show the distribution of useful UHR images received daily. The ideal situation is to obtain two useful QuikSCAT observations per day all the time; however this occurred only 25.7 % and 19.1 % of the time in the ATL and the EP, respectively (see Fig. 3.9). Nevertheless, at least one useful UHR image is obtained daily 60.5 % (ATL) and 76.7 % (EP) of the time (values obtained by adding percentages from 1/1, 1/2, and 2/2 slices from Fig. 3.9 for each basin). Perhaps, having at least two scatterometers on different platforms all revolving on polar orbits around the globe would solve these fairly low results. In any case, judging the usefulness of an image is a subjective task and relies heavily on the analyst's experience of interpreting a QuikSCAT wind fields UHR image. Therefore, it could be possible to get more useful images per day depending on the analyst's experience of interpreting wind field patterns.

3.4.1 Results obtained from Seawinds on QuikSCAT and ADEOS II-year 2003

As mentioned in Section 3.3, two scatterometers were operational during the year 2003 (Seawinds on QuikSCAT and on ADEOS II). Both devices provided the same wind products at the same daily rate. The orbit phasing ensured that each instrument would observe the same location at different local-time of day. As a result, the amount of useful daily UHR images for TC analysis ideally is doubled. Fig. 3.10 shows the results obtained for that year. As expected, a maximum of four useful UHR images was available daily (in a few cases up to five). In fact, 15.5 % of the time in the ATL basin for instance, four out of four UHR images received daily are useful to the analyst (see top pie chart of Fig. 3.10). Both pie charts on this figure also show that close to 45 % of the time, two or more useful UHR images are available daily, versus 19.1 and 25.7 % (for the EP and ATL basins, respectively—see Fig. 3.9) when only one scatterometer is available. As one might expect, two scatterometers measuring wind fields over the ocean and operating simultaneously around the globe provide more critical data on a daily basis to TC analysts.

Though prone to noise and rain contamination, the 2.5 km ultra-high resolution images from SeaWinds on QuikSCAT reveal mesoscale features which are not visible in standard 25 km wind fields. Thus, UHR images can be used to identify more easily and accurately TC eye locations. Poor results may still be obtained at times. However, these are mostly due to under-developed TC stage or to the analyst's capability to identify TC characteristics. By dividing the UHR images into two categories based on the analyst's confidence level of finding the eye center location, QuikSCAT's effectiveness in helping to identify these critical locations is more evident.

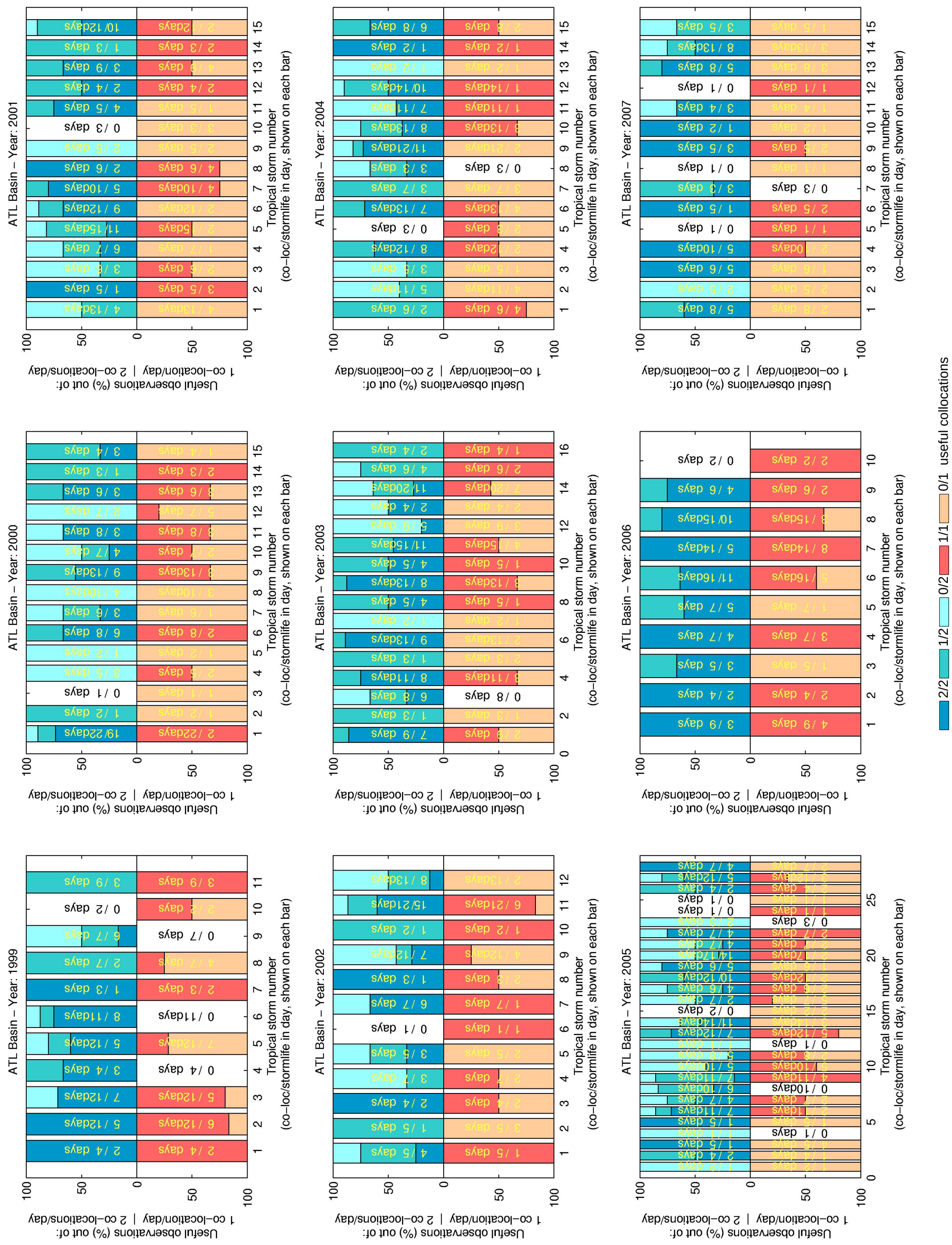

Figure 3.8: Bar graphs showing the amount of useful QuikSCAT observations received per TC daily for the ATL basin from 1999 to 2007. On each bar graph, two sets of data are shown: upper bars show statistics for two co-located images obtained daily; lower bars show statistics when only one co-located image is obtained daily. The former scenario has 3 cases where possibly both obtained images are useful to the analyst, only one is or none of them are. For the latter, either the received image is useful to the analyst or not. Each of these possibilities is represented on the bar graph in percent for each TC.

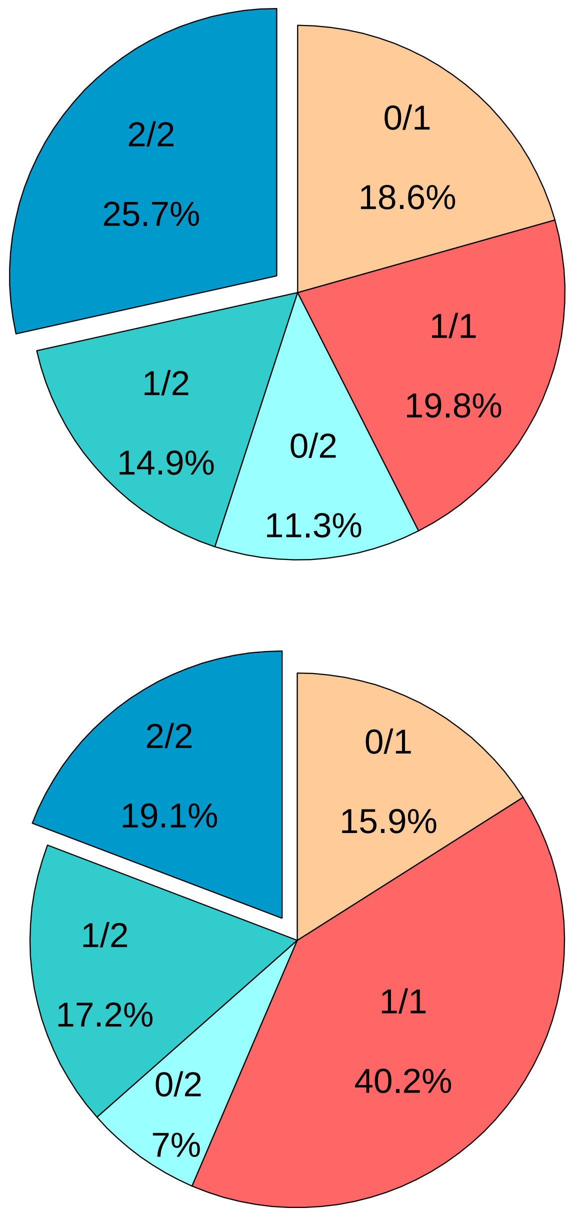

Figure 3.9: Pie charts displaying how often useful UHR images are retrieved for TCs of all QuikSCAT images available daily, as noted on each slice (top: ATL and bottom: EP; years 1999-2007 combined). Up to two images can be retrieved per day though in many cases only a single image per day is available. The exploded slices show that two useful (for TC eye identification) out of two available images per day were obtained for 25.7 % (ATL) and 19.1 % (EP) of the time between 1999 and 2007.

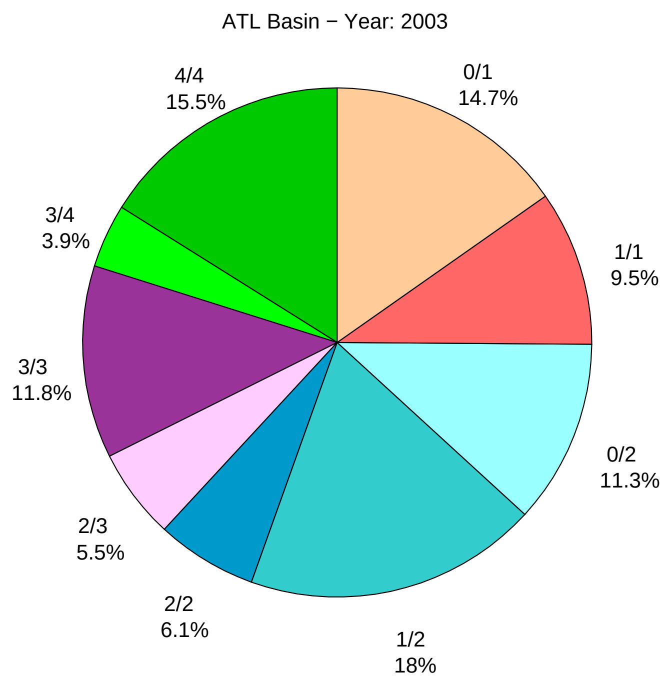

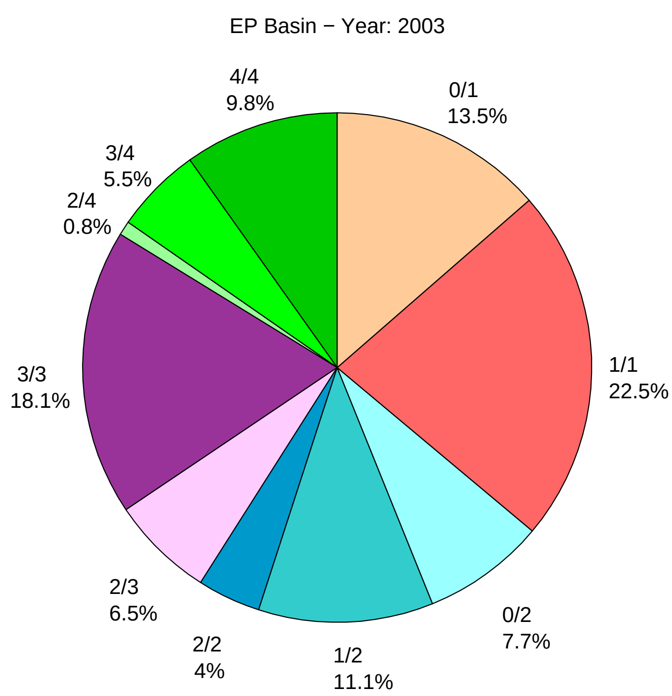

Figure 3.10: Pie charts displaying how many useful UHR images are retrieved per day for the year 2003. Next to each slice, the number of useful images per daily colocated images obtained is provided, as well as the percentage it represents. The top and bottom charts show results for the ATL and EP basins, respectively. During this year, two scatterometers (Seawinds on ADEOS II and on QuikSCAT) provided UHR images simultaneously which increased temporal coverage. It is thus possible to obtain up to 4 useful UHR images per TC per day.

Chapter 4

Wind radii Estimation: preliminary analysis

Wind radii are valuable metrics used by NHC to help estimate the size, storm surge, storm intensity, and possible impact of a given TC. Wind radii estimates are derived from instruments placed on aircraft which fly through storms in an alpha pattern (see Fig. 4.1) as far as 105 nautical miles from the eye center [18].

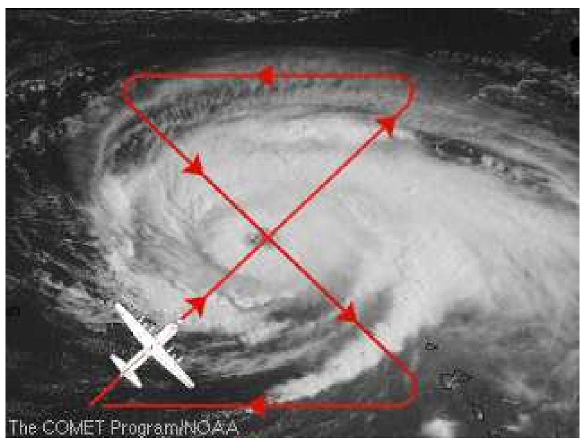

Figure 4.1: This figure shows the usual path taken by jet aircraft while flying over a TC. Such a path is called an alpha pattern and is performed at least twice each time an aircraft flies over a storm. Along this path, the aircraft drops several GPS dropwindsondes and uses on-board radiometers and scatterometers to provide critical TC measurements, which are then sent in near-real time to NHC TC analysts.

With the use of GPS dropwindsonde and on-board radiometers/scatterometers, these aircraft are capable of measuring atmospheric pressure, temperature, humidity, and wind speed and direction along their path. These measurements can be instantly sent to the TC forecasters at the NHC for immediate analysis.

Because these aircraft cannot fly over the whole storm, resolution of the aircraft-inferred wind speed field can be low in a given quadrant. Furthermore, when TCs are out of reach from these aircraft, forecasters rely heavily on the relatively few buoys scattered over the Atlantic ocean, and scatterometers to estimate wind radii. The latter can substantially supply more data for a given storm compared to buoys. NHC estimates of wind radius are subjective and therefore it is of interest to use automated algorithms to estimate wind radii using QuikSCAT UHR wind products and analyze their performance. To do this, wind radii obtained from QuikSCAT are first compared with H*Wind. They are then compared with the Extended Best-Track data set. These two sets of data are defined in their respective sections.

4.1 Comparison of QuikSCAT UHR wind radii with H*wind data

The hurricane research division (part of NOAA) has been working since 1996 on a project called H*wind. The purpose of this project is to develop an integrated tropical cyclone observing system using data gathered from various platforms (including QuikSCAT). The experimental product includes wind data (surface speed and direction fields) which are mostly used for research purposes. A detailed description of this project is provided in [19]. Figure 4.2 illustrates an example of H*Wind speed field for Tropical Cyclone Ike on 6 September 2008 at 2249 UTC in the ATL basin. Note how smooth the wind speed field appears. Though this does not really reflect reality, H*wind is still considered to be pretty close to the truth with a 10 to 20 % error. Note that this error margin is attainable only when aircraft data are used in the generation of H*wind data, which is only possible when TCs are reachable from land-based aircraft. This limits the number of possible spatial and temporal collocations between QuikSCAT passes and H*wind; in fact, between 1999 and 2008, only 47 Tropical Cyclone cases were successfully collocated (collocation processing was performed at the University of North Carolina at Asheville [20]) for the ATL basin where H*wind is mainly available. Table 4.1 summarizes the number of collocations per storm type. It is important to note that QuikSCAT data was excluded in the generation of the 47 collocated H*wind data so as to provide a fair comparison between the two products.

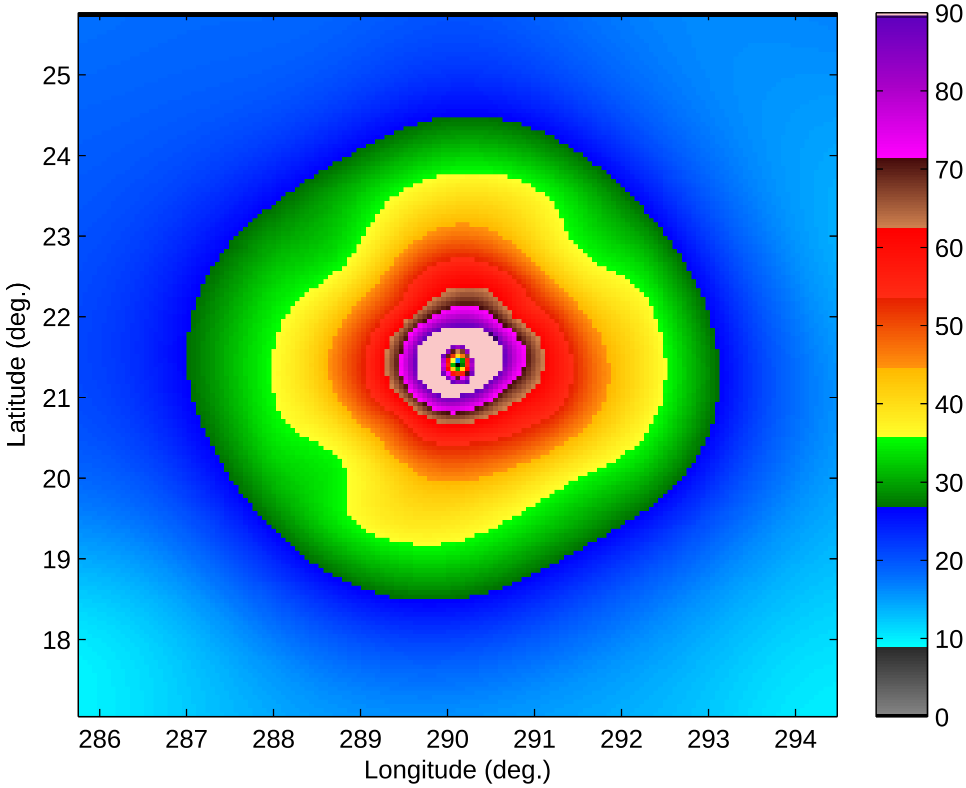

Figure 4.2: This figure illustrates H*wind wind speed estimation of TC Ike on 6 September 2008 at 2249 UTC in the ATL basin. This plot was generated using data from [20]. Color scale is in knots.

Due to QuikSCAT's limitations in retrieving accurate high wind speeds, most of the analysis hereafter is performed on Tropical Storm cases. A few examples of Hurricane type TCs are provided to illustrate QuikSCAT performance in extreme wind speed situations.

4.1.1 Visual analysis of a few Tropical Storm (TS) cases

Visual analysis of TC cases consists of plotting and comparing H*wind and QuikSCAT UHR wind speed field for a given quadrant. Note that only the North East (NE) quadrant of each storm is analyzed in this thesis. Each figure contains four plots; two plots represent H*wind and QuikSCAT wind speed fields; the other two are scatter plots of QuikSCAT UHR wind speed versus distance from the eye, and H*wind wind speed versus distance from the eye overlaid with QuikSCAT, respectively. Note that for the latter, only the four QuikSCAT

Table 4.1: Number of H*wind/QuikSCAT collocations per storm type between 1999 and 2008

TC type	Collocations
Tropical Depression	0
Tropical Storm	10
Hurricane Cat 1	9
Hurricane Cat 2	6
Hurricane Cat 3	5
Hurricane Cat 4	12
Hurricane Cat 5	5
Total	47

UHR wind speed maxima for each distance are overlaid with H*wind: since wind radii are determined by finding the maximum possible wind speeds at a given radius, QuikSCAT UHR wind radii can then be determined visually based solely on the four maxima for each distance. These wind speed maxima, however, should be interpreted with caution since UHR wind products are inherently noisy and may be rain contaminated.

TS Fay on 21 August 2008 at 1042 UTC

A total of 5 out the 10 collocated TS cases are chosen to illustrate the results obtained for Tropical Storms. In Fig. 4.3, H*wind and QuikSCAT wind speeds (see lower right plot) show a fairly good correlation as far as 50 nmi. Beyond this distance, H*wind speed versus distance decreases monotonically, while QuikSCAT speed versus distance does not. Justification for such latter behavior can be attributed to overestimation of wind speed in high rain rate areas (as depicted in top right plot of Fig. 4.3 about 100 nmi NE from the TC eye center). Furthermore, isolated thunderstorms of variable size over the ocean can be present in the proximity of a TC core; these can be seen about 250 nmi NE and 300 nmi slightly SE of the TC eye center. If the effects of these mesoscale weather systems are ignored, the 34-kt wind radius estimated from QuikSCAT should be very similar to H*wind 34-kt wind radius.

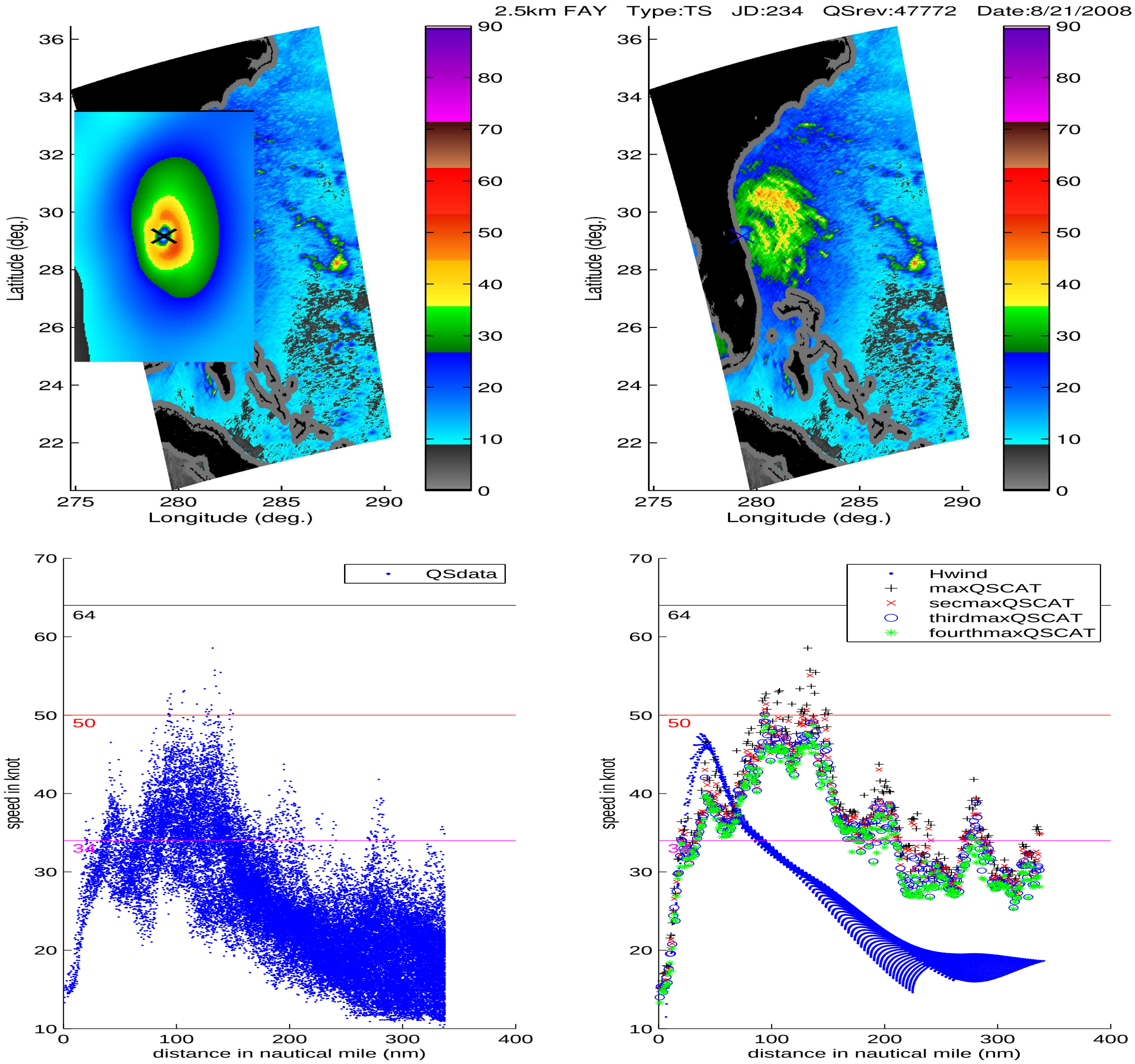

Figure 4.3: Plots of H*wind and QuikSCAT UHR wind speed fields for TS Fay on 21 August 2008 at 1042 UTC. The upper left and right images show, respectively, H*wind overlaid with QuikSCAT UHR wind speed field, and QuikSCAT UHR wind speed field alone. The lower left plot shows a scatter plot of QuikSCAT UHR wind speed only versus distance from the eye. The lower right plot is a scatter plot of H*wind speed versus distance from the eye overlaid with the top four wind speed maxima for each distance from QuikSCAT.

TS Ophelia on 9 September 2005 at 2337 UTC

TS Ophelia (see Fig. 4.4) is another example where overestimation of wind speed due to high rain rate is possible at about 120 nmi slightly NE from the eye center. If this feature is ignored, the 34- and 50-kt wind radii from QuikSCAT are relatively close to H*wind's.

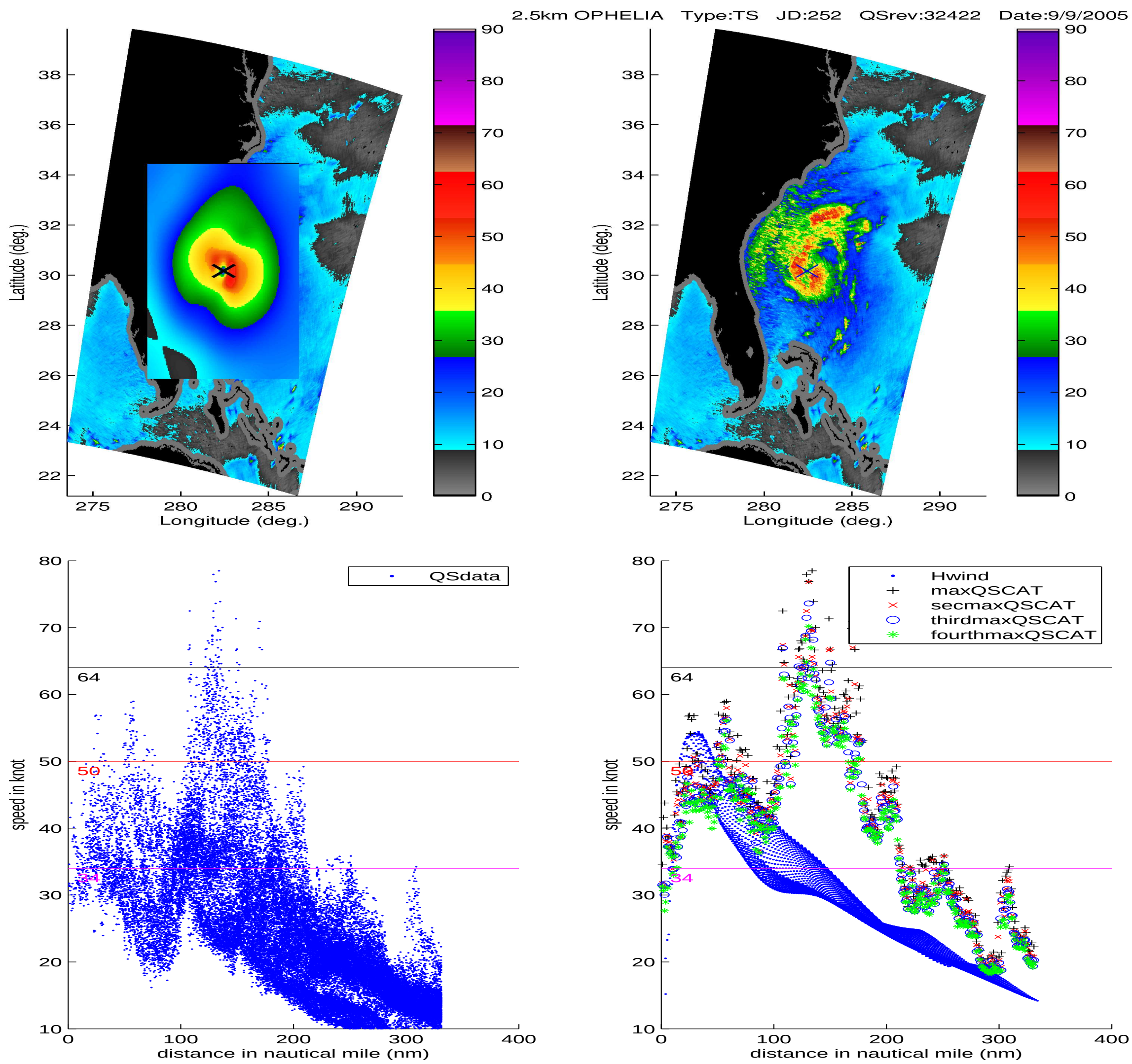

Figure 4.4: Plots of H*wind and QuikSCAT UHR wind speed fields for TS Ophelia on 9 September 2005 at 2337 UTC. The upper left and right images show, respectively, H*wind overlaid with QuikSCAT UHR wind speed field, and QuikSCAT UHR wind speed field alone. The lower left plot shows a scatter plot of QuikSCAT UHR wind speed only versus distance from the eye. The lower right plot is a scatter plot of H*wind speed versus distance from the eye overlaid with the top four wind speed maxima for each distance from QuikSCAT.

TS Bonnie on 11 August 2004 at 2338 UTC

TS Bonnie on 11 August 2004 was under-developed and much smaller compared to the two previous discussed TS cases. This time, QuikSCAT wind speed versus distance (see lower right scatter plot of Fig. 4.5) yields higher wind speed overall, based exclusively on the top four maxima for each distance, compared to H*wind. This may be due to rain

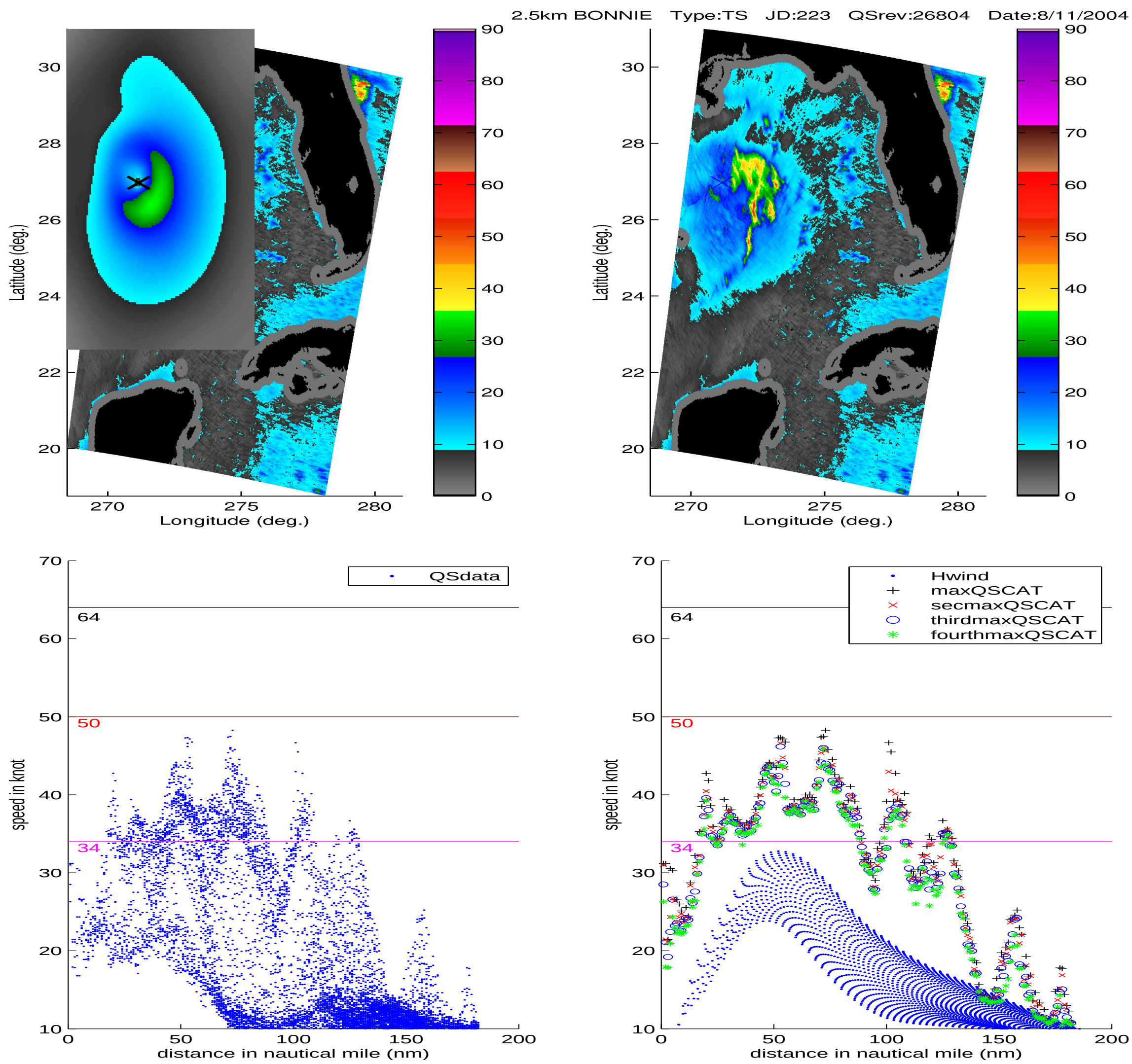

Figure 4.5: Plots of H*wind and QuikSCAT UHR wind speed fields for TS Bonnie 11 August 2004 at 2338 UTC. The upper left and right images show, respectively, H*wind overlaid with QuikSCAT UHR wind speed field, and QuikSCAT UHR wind speed field alone. The lower left plot shows a scatter plot of QuikSCAT UHR wind speed only versus distance from the eye. The lower right plot is a scatter plot of H*wind speed versus distance from the eye overlaid with the top four wind speed maxima for each distance from QuikSCAT.

bands, though this cannot be confirmed. We note that QuikSCAT shows a much more complicated wind field than suggested by H*wind. If these wind speeds are close to the surface truth, QuikSCAT data yields a 34-kt wind radius while H*wind does not. In any case, it is interesting to note that both scatter plots have very similar overall curve shape.

TS Dolly on 22 July 2008 at 1200 UTC

TC Dolly has some very similar characteristics to previously described TS Fay, TS Ophelia, and TS Bonnie. There are some noticeable areas of high rain rates associated with isolated thunderstorms far from TC Dolly's core, which can be ignored for wind radii estimation purposes. Once they are, the shape of QuikSCAT wind speed curve correlates very well with H*wind's (see lower right scatter plot of Fig. 4.6). By visually inspecting this plot, the wind radii estimated either by QuikSCAT or H*wind yield about the same results.

TS Hanna on 5 September 2008 at 1052 UTC

At first glance, the storm sizes for TS Hanna shown on the upper plots of Fig. 4.7 by both H*winds and QuikSCAT agree well. However, a closer look to the lower right plot of this figure reveals poor correlation between the two data sets. Interesting insights are that QuikSCAT is providing a 64-kt wind radius while H*wind shows no winds over 64 kt; the 50-kt wind radii from both data sets are very different; the 34-kt wind radii, on the other hand, are somewhat similar if we ignore the outer rain bands which cause QuikSCAT to overestimate wind speed.

NHC provided a forecast advisory at 0900 UTC for TS Hanna and reported the following wind radii in that quadrant: a 34-kt wind radius of 275 nmi, a 50-kt wind radius of 90 nmi, and no 64-kt wind radius. The fact that QuikSCAT reported wind speeds equal or greater than 64 kt is likely due to rain band effects. The peaks shown in the lower right plot of Fig. 4.7 between 100 and 200 nmi should be ignored. The QuikSCAT 50-kt wind radius is, as a result, closer to H*wind and the NHC reported 50-kt wind radius. It is interesting to note that the QuikSCAT 34-kt estimated wind radius is very similar to the NHC reported radius, while H*wind underestimates it a bit.

4.1.2 Visual analysis of Hurricane type TCs

Though QuikSCAT was not designed to retrieve wind speed well above 50-kt, a few hurricane cases are shown in this subsection to illustrate QuikSCAT's performance of estimating wind radii in such condition.

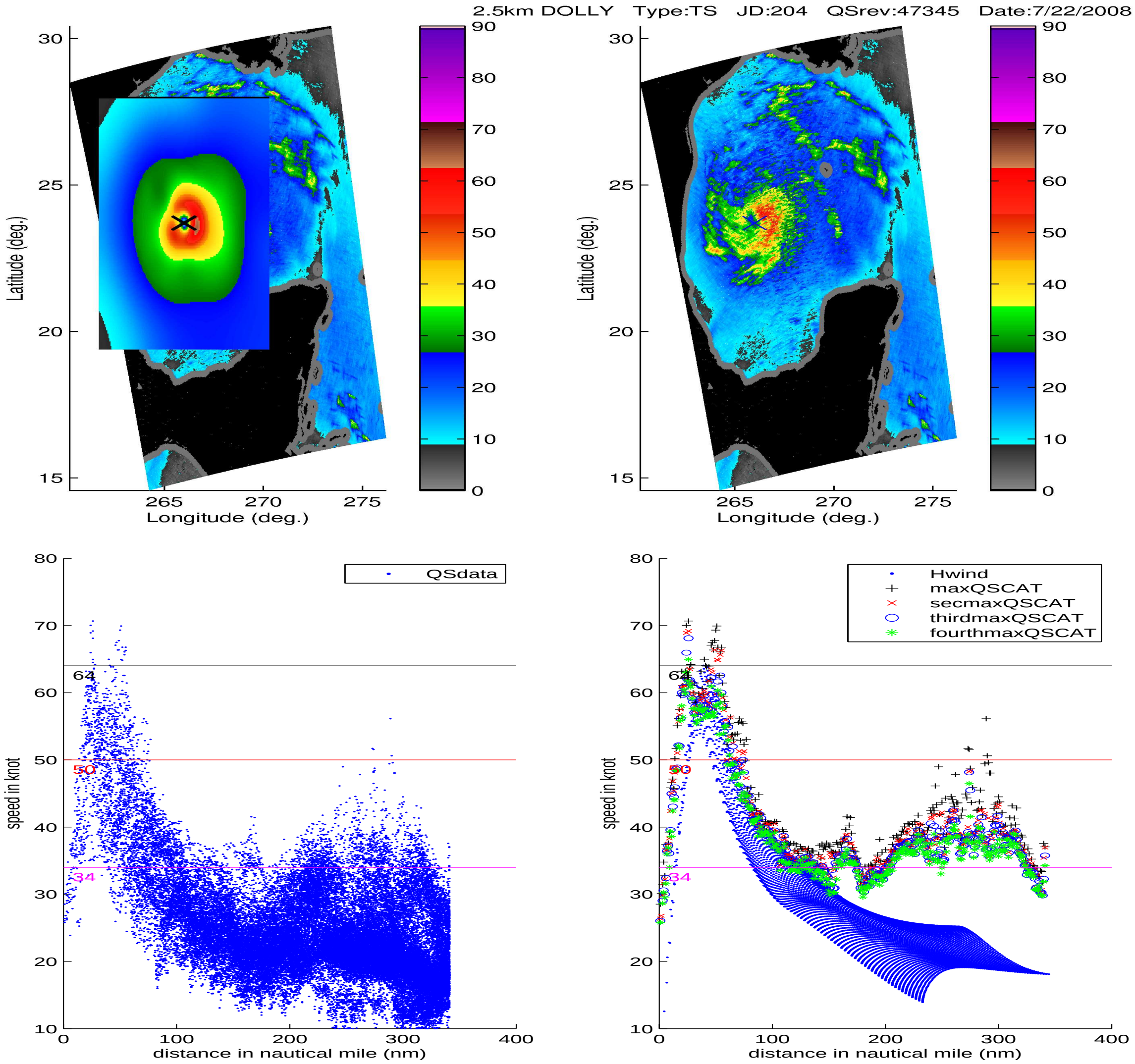

Figure 4.6: Plots of H*wind and QuikSCAT UHR wind speed fields for TS Dolly on 22 July 2008 at 1200 UTC. The upper left and right images show, respectively, H*wind overlaid with QuikSCAT UHR wind speed field, and QuikSCAT UHR wind speed field alone. The lower left plot shows a scatter plot of QuikSCAT UHR wind speed only versus distance from the eye. The lower right plot is a scatter plot of H*wind speed versus distance from the eye overlaid with the top four wind speed maxima for each distance from QuikSCAT.

H1 Bertha on 11 July 2008 at 2227 UTC

In the case of Hurricane Bertha on 11 July 2008 at 2227 UTC, QuikSCAT underestimates the wind speed beyond 50 nmi from the eye center according to the lower right plot of Fig. 4.8, assuming H*wind is correct in this example. No real explanation can be given at this point for such behavior unless the H*wind data in this case are not accurate. In fact,

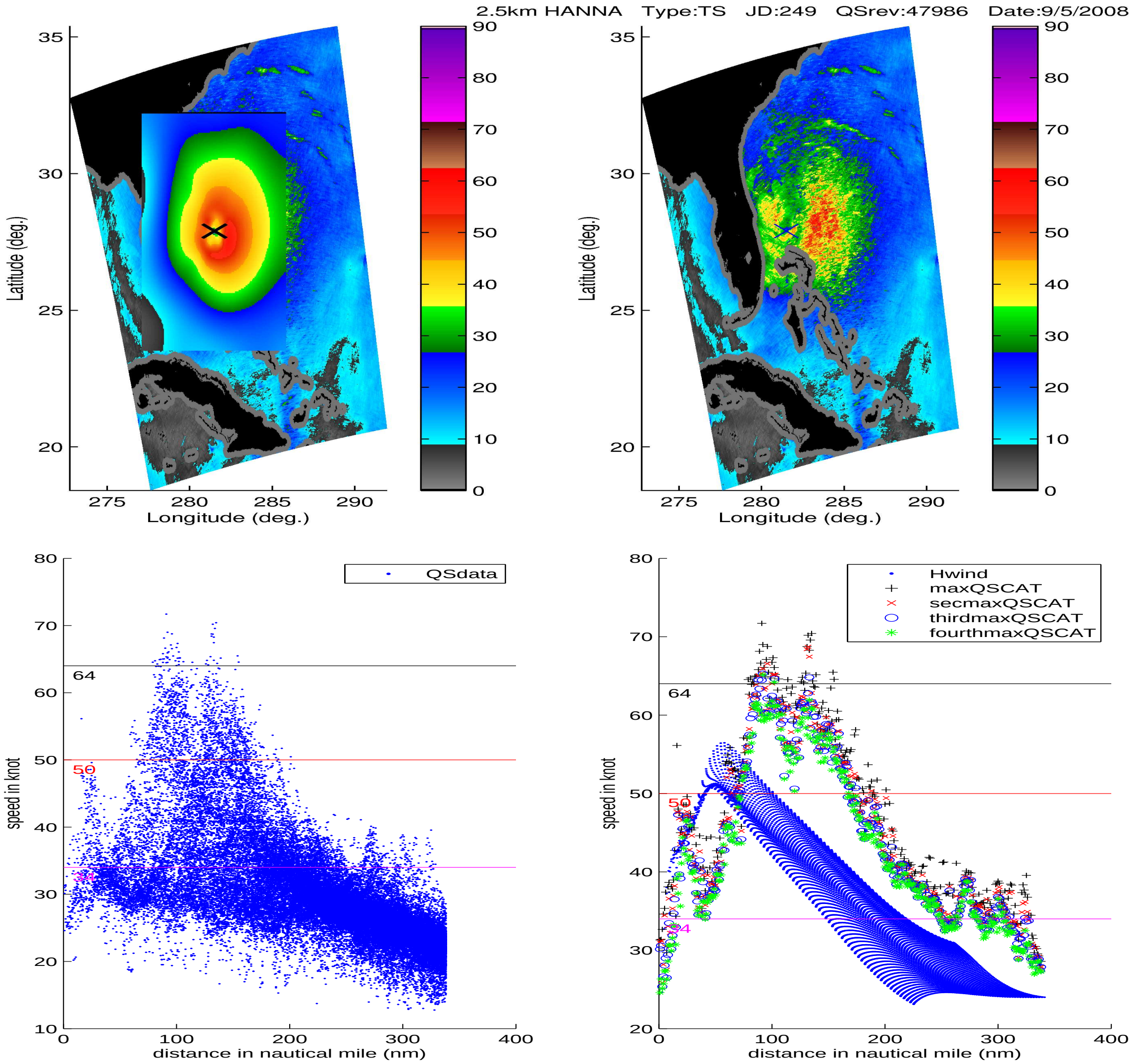

Figure 4.7: Plots of H*wind and QuikSCAT UHR wind speed fields for TS Hanna on 5 September 2008 at 1052 UTC. The upper left and right images show, respectively, H*wind overlaid with QuikSCAT UHR wind speed field, and QuikSCAT UHR wind speed field alone. The lower left plot shows a scatter plot of QuikSCAT UHR wind speed only versus distance from the eye. The lower right plot is a scatter plot of H*wind speed versus distance from the eye overlaid with the top four wind speed maxima for each distance from QuikSCAT.

an NHC forecast advisory given for H1 Bertha on 11 July 2008 at 2100 UTC (1.5 hour prior to QuikSCAT pass over the storm) reported the following wind radii for the NE quadrant: 120, 60, and 30 nmi for the 34-,50-, and 64-kt wind radii, respectively. These wind radii surprisingly agree very well with QuikSCAT wind radii derived from the lower right plot of Fig. 4.8 but disagree with H*wind.

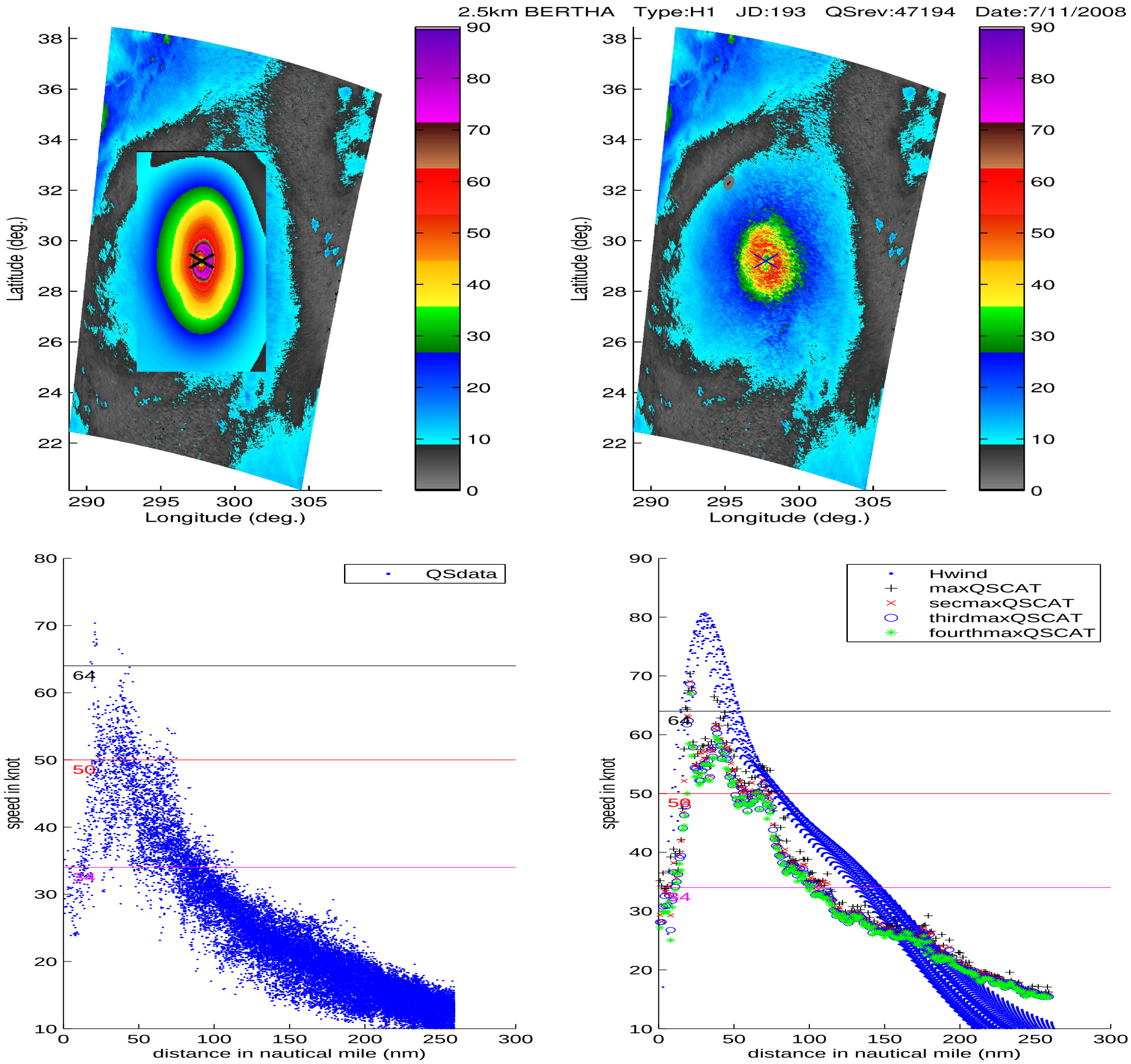

Figure 4.8: Plots of H*wind and QuikSCAT UHR wind speed fields for H1 Bertha on 11 July 2008 at 2227 UTC. The upper left and right images show, respectively, H*wind overlaid with QuikSCAT UHR wind speed field, and QuikSCAT UHR wind speed field alone. The lower left plot shows a scatter plot of QuikSCAT UHR wind speed only versus distance from the eye. The lower right plot is a scatter plot of H*wind speed versus distance from the eye overlaid with the top four wind speed maxima for each distance from QuikSCAT.

H2 Jeanne on 24 September 2004 at 2259 UTC

The collocated wind speed fields of H*wind and QuikSCAT for TC Jeanne given in Fig. 4.9 show a high correlation between the two data sets even though Jeanne was considered a hurricane cat 2 (sustained wind speed between 83-96 knots). This is somewhat unusual since QuikSCAT have difficulty retrieving such high wind speeds. High rain rates may have positively biased QuikSCAT wind speed estimation, though it is not confirmed.

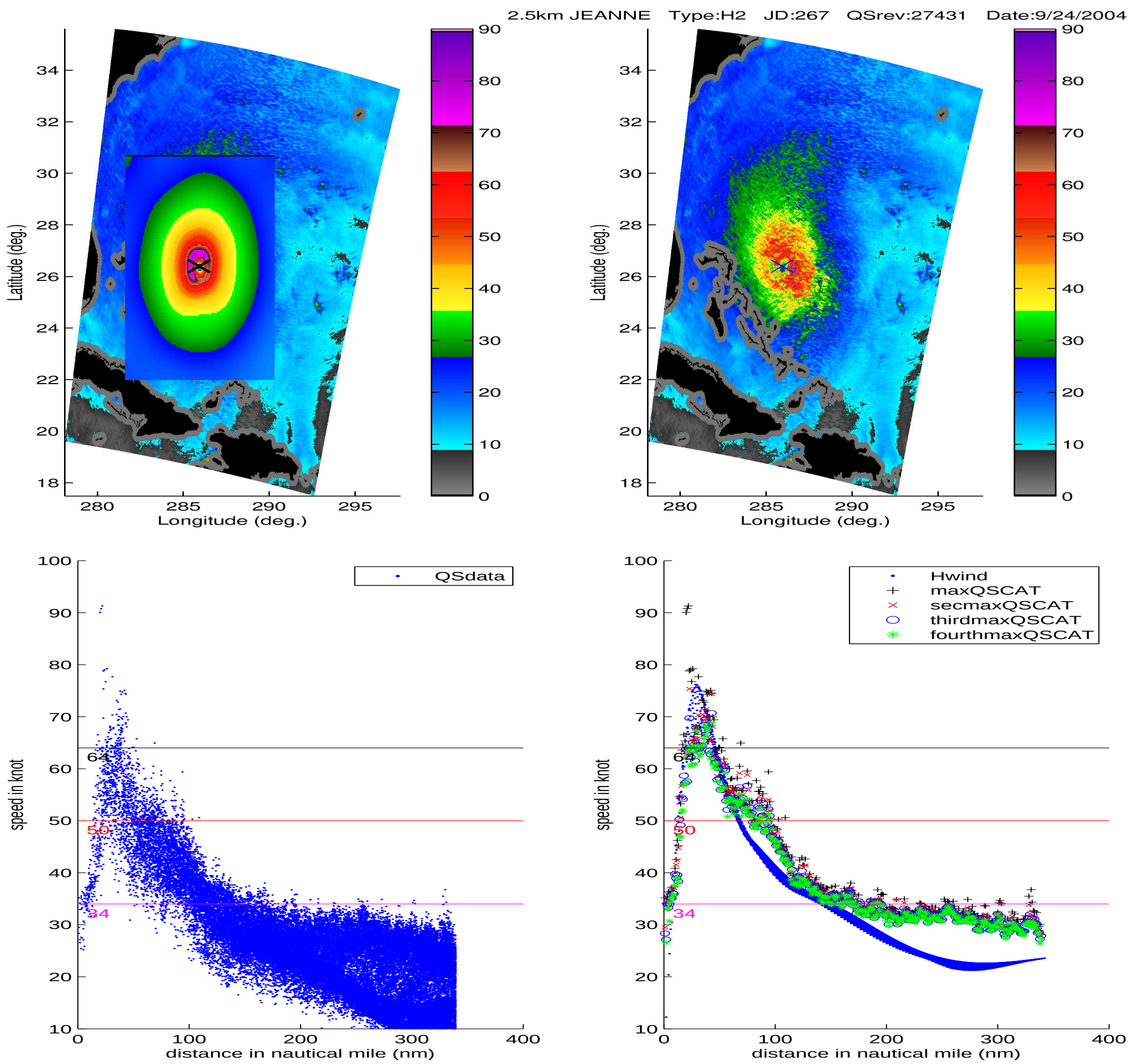

Figure 4.9: Plots of H*wind and QuikSCAT UHR wind speed fields for H2 Jeanne on 24 September 2004 at 2259 UTC. The upper left and right images show, respectively, H*wind overlaid with QuikSCAT UHR wind speed field, and QuikSCAT UHR wind speed field alone. The lower left plot shows a scatter plot of QuikSCAT UHR wind speed only versus distance from the eye. The lower right plot is a scatter plot of H*wind speed versus distance from the eye overlaid with the top four wind speed maxima for each distance from QuikSCAT.

H3 Katrina on 28 August 2005 at 0016 UTC

This example of Hurricane Katrina on 28 August 2005 at 0016 UTC (see Fig. 4.10) shows what it is expected of QuikSCAT in such extreme wind conditions. In this case, QuikSCAT wind speeds are severely underestimated compared to H*wind for most of the storm core in the NE quadrant. However, NHC reported, 3 hours before and after this QuikSCAT pass, the following wind radii: a 34-kt wind radius of 140 nmi in both instances, 50-kt wind radii ranging between 60 and 75 nmi, and 64-kt wind radii ranging between 40 and 60 nmi. Once again, these numbers (except for the 64-kt radius) agree well with QuikSCAT wind speed shown in the lower right plot of Fig. 4.10.

H4 Fabian on 4 September 2003 at 2236 UTC

This last example of Hurricane cat 4 Fabian shows good correlation between H*wind and QuikSCAT (see Fig. 4.11). However, QuikSCAT wind speed is underestimated between 20 and 50 nmi, which most likely corresponds to the eye wall where wind speeds are the highest. In any case, the 34- and 50-kt wind radii estimated from both data sets are very comparable.

These results show that it is possible to estimate wind radii even in extreme conditions (i.e. hurricane categories 1 through 4). It has been shown that high rain rates are a real problem for estimating the wind radii since wind speed is often overestimated when heavy rain is present. It is now desired to perform similar analysis using the Extended Best-Track data set instead of H*wind as ground truth for wind radii estimation purposes.

4.2 Comparison of QuikSCAT UHR wind radii with Extended Best-Track data

As mentioned in Chapter 2 Section 2.3.1, the NHC performs yearly TC post-season analysis of all information available and creates a data set called Best-Track (BT), which is made available to the scientific community and the public. The data set provides the eye location, maximum sustained wind speed and atmospheric pressure at the eye center every six hours over any TC lifetime within the Atlantic and Eastern Pacific basins. It does not, however, provide wind radii information, though this metric can be found in all NHC forecast advisories while TCs are tracked.

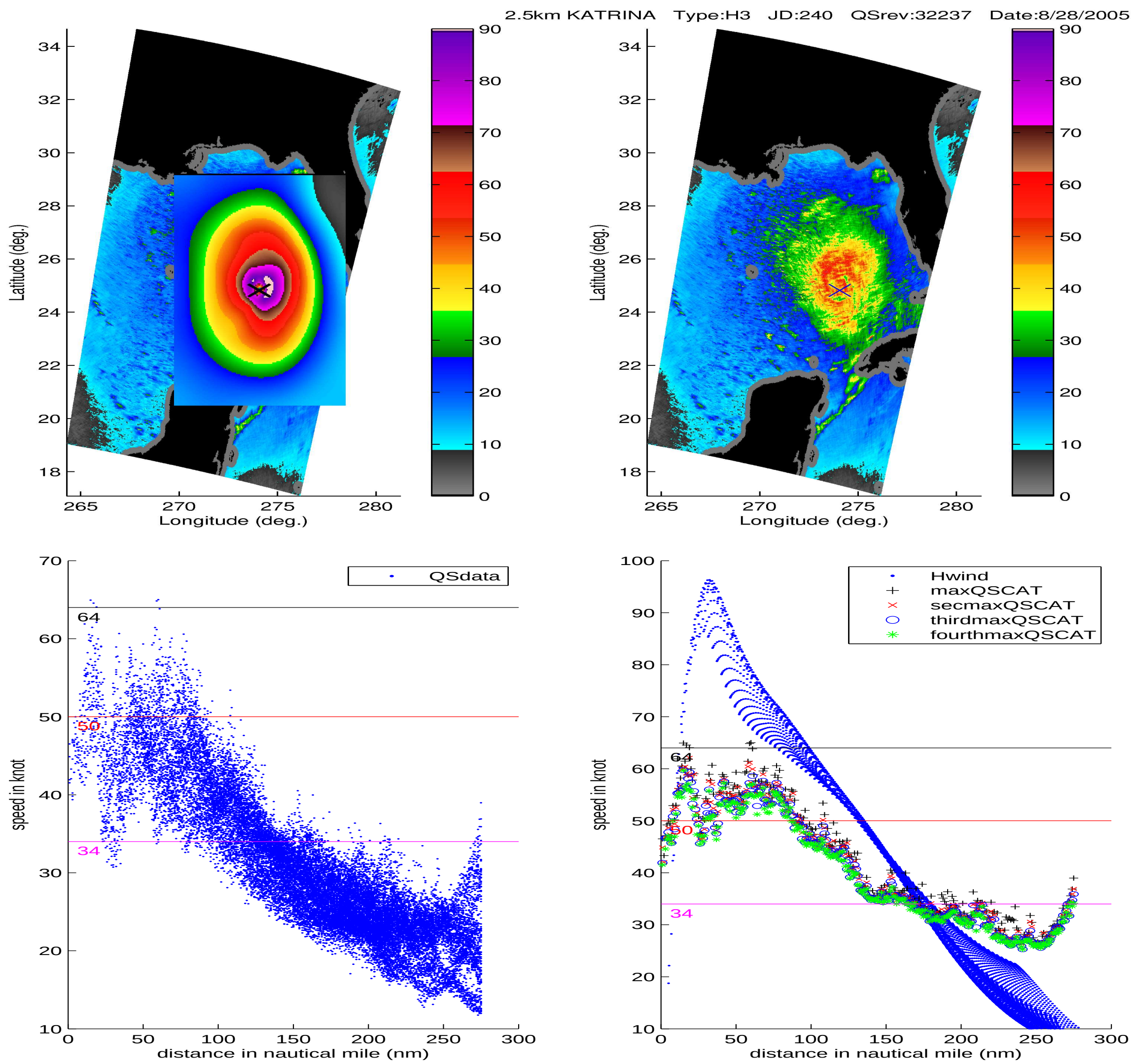

Figure 4.10: Plots of H*wind and QuikSCAT UHR wind speed fields for H3 Katrina on 28 August 2005 at 0016 UTC. The upper left and right images show, respectively, H*wind overlaid with QuikSCAT UHR wind speed field, and QuikSCAT UHR wind speed field alone. The lower left plot shows a scatter plot of QuikSCAT UHR wind speed only versus distance from the eye. The lower right plot is a scatter plot of H*wind speed versus distance from the eye overlaid with the top four wind speed maxima for each distance from QuikSCAT.

M. DeMaria [21], with partial support from the Risk Prediction Initiative [22], prepared a supplement to BT called the Extended Best-Track (EBT). This data set contains, in addition to what BT data already provides, radius of maximum wind speed, eye diameter, pressure of the outer closed isobar (hPa), radius of the outer closed isobar (nmi), and radii of 34-,50-,64-kt for each quadrant of the TCs. Since EBT provides these metrics every six hours during any TC lifetime, 146 collocations for the ATL basin (1999-2007) between EBT data

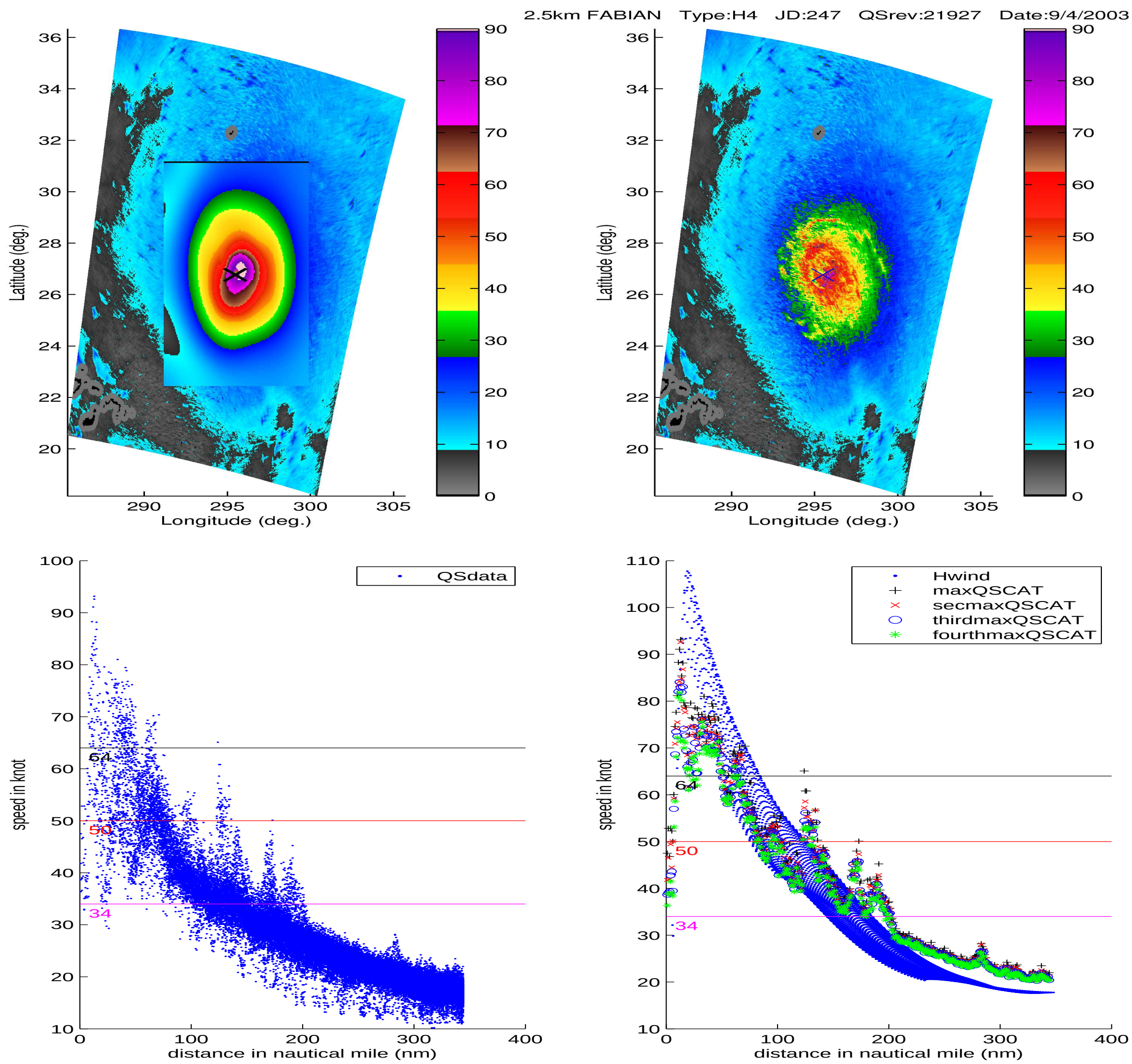

Figure 4.11: Plots of H*wind and QuikSCAT UHR wind speed fields for H4 Fabian on 4 September 2003 at 2236 UTC. The upper left and right images show, respectively, H*wind overlaid with QuikSCAT UHR wind speed field, and QuikSCAT UHR wind speed field alone. The lower left plot shows a scatter plot of QuikSCAT UHR wind speed only versus distance from the eye. The lower right plot is a scatter plot of H*wind speed versus distance from the eye overlaid with the top four wind speed maxima for each distance from QuikSCAT.

set and QuikSCAT UHR are possible. However, land contamination and under-developed TC conditions reduce the number of interesting collocations down to 46. Furthermore, estimated wind radii reported in the EBT are considered more reliable west of 55 longitude, where aircraft data is usually available. 41 out of the 46 collocations follow this criteria. Analysis for some of these cases is found in the following subsections.

4.2.1 Visual analysis of EBT Tropical Storm cases

Three cases are used to illustrate results obtained for the few TS cases available. Plots are very similar to those given in Section 4.1, except that the scatter plot of the four QuikSCAT wind speed maxima for each distance is overlaid with vertical lines showing the three EBT wind radii. The first example shown in Fig. 4.12 reflects a common problem we encounter in this analysis where wind speed around the eye wall are most of the time underestimated. This may explain the absence of the 50-kt wind radius from QuikSCAT. Its 34-kt wind radius, however, matches very well with EBT's.

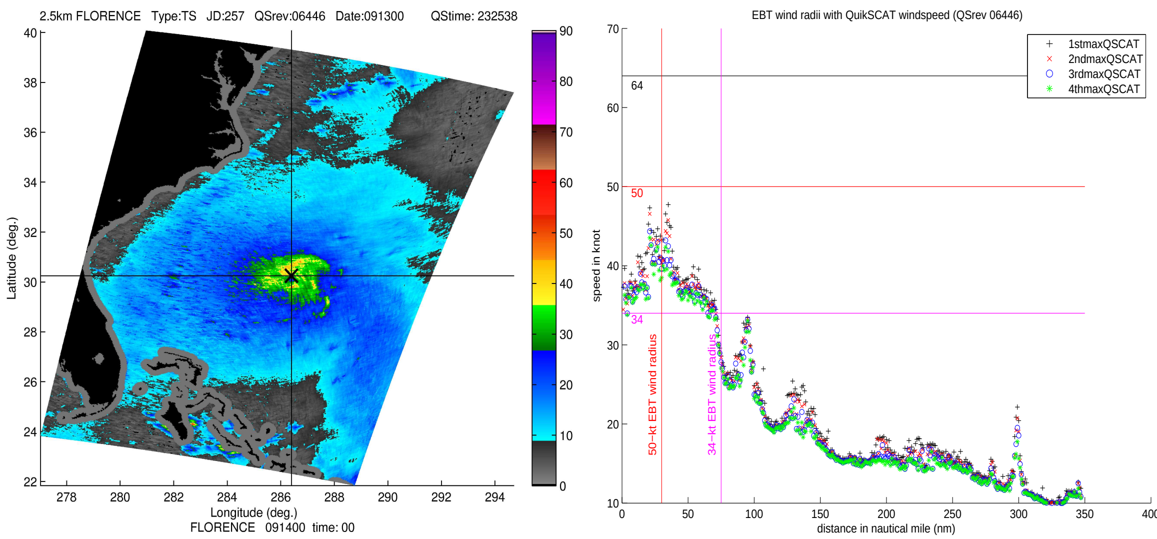

Figure 4.12: TS Florence on 13 September 2000 at 2325 UTC. The left plot shows QuikSCAT UHR wind speed field. Note as part of its title the time of QuikSCAT pass over that TC. This can be compared with the time of the collocated estimated wind radii from EBT shown below this plot. The right plot is a scatter plot of the four QuikSCAT wind speed maxima for each distance. The three vertical lines correspond to the three collocated EBT wind radii.

Two cases from TS Ophelia on 13 September 2005 (see Fig. 4.13) show the 34- as well as the 50-kt EBT wind radii matching very well with QuikSCAT's. It is hard to interpret why at times QuikSCAT has no difficulty estimating wind speeds close to or above 50-kt while at other times the estimates are inaccurate. For TS Ophelia, it is not clear whether estimates of the wind speed equal or above 50-kt are accurate or overestimated due to high rain rate effects on QuikSCAT backscatter measurements.

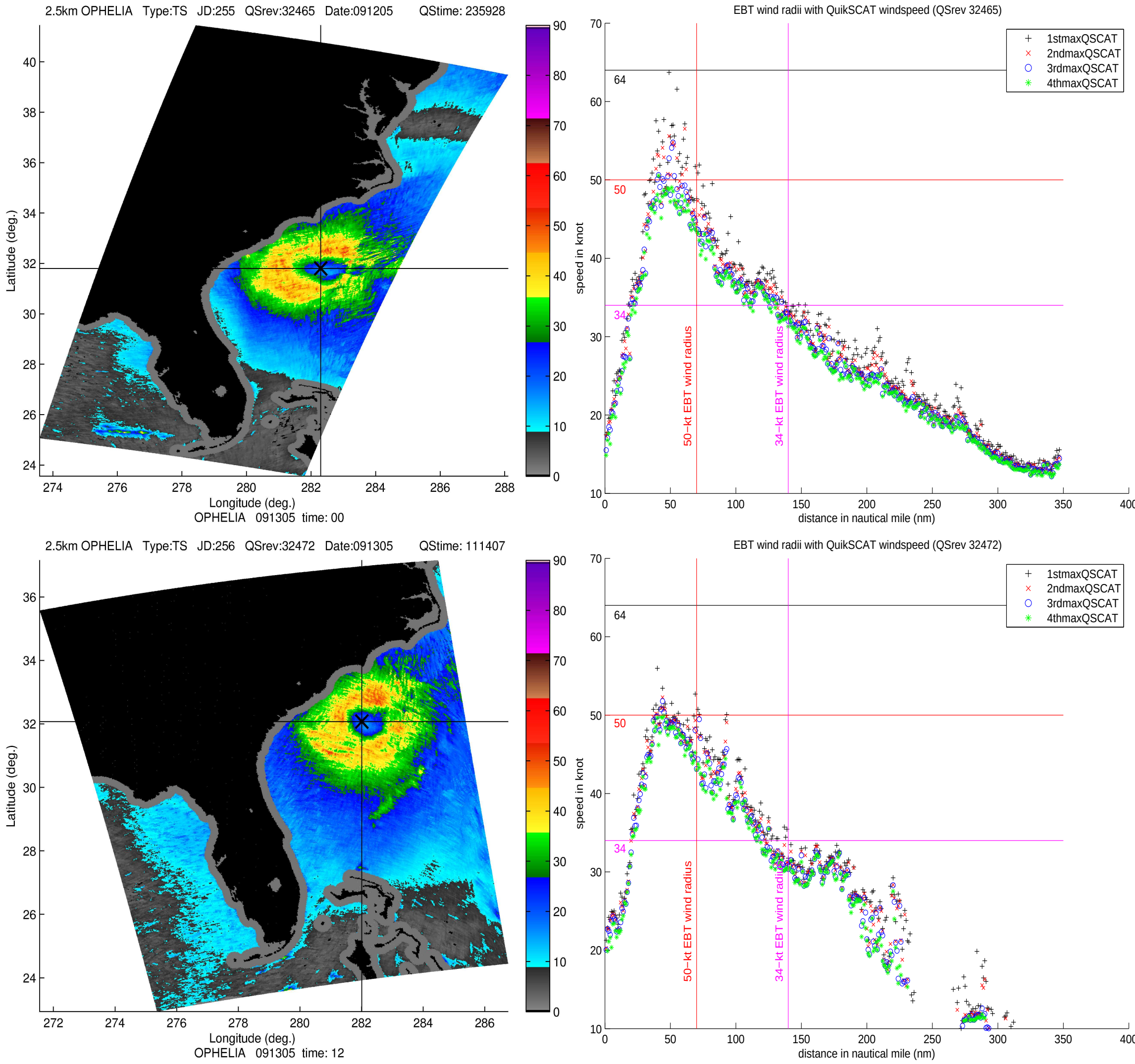

Figure 4.13: TS Ophelia on 13 September in 2005. The upper left and bottom left plots show QuikSCAT UHR wind speed field. Note as part of their title the time of QuikSCAT pass over that TC. This can be compared with the time of the collocated estimated wind radii from EBT shown below these plots. The upper right and bottom right plots are scatter plots of the four QuikSCAT wind speed maxima for each distance. The three vertical lines correspond to the three collocated EBT wind radii.

4.2.2 Visual analysis of a few Hurricane cases

Due to the relatively few hurricane cases available out of the 41 collocations between EBT and QuikSCAT, a single case is given per hurricane category. However, there are no category 2 or 3 cases presented due to lack of collocations. Hurricane Dean (cat 1) case (see Fig. 4.14) provides some interesting results. The 34- and 64-kt wind radii from QuikSCAT correlate fairly well with EBT's except the 50-kt, which is underestimated by approximately 40 nmi. There is no clear justification as to why such results are obtained. However, it is interesting to note that wind radii reported by hurricane analysts (i.e. EBT wind radii) are subjective estimates and may not indicate direct wind radius measurements from any instrument; a subjective margin of error may have been added to the actual wind speed measurements received.

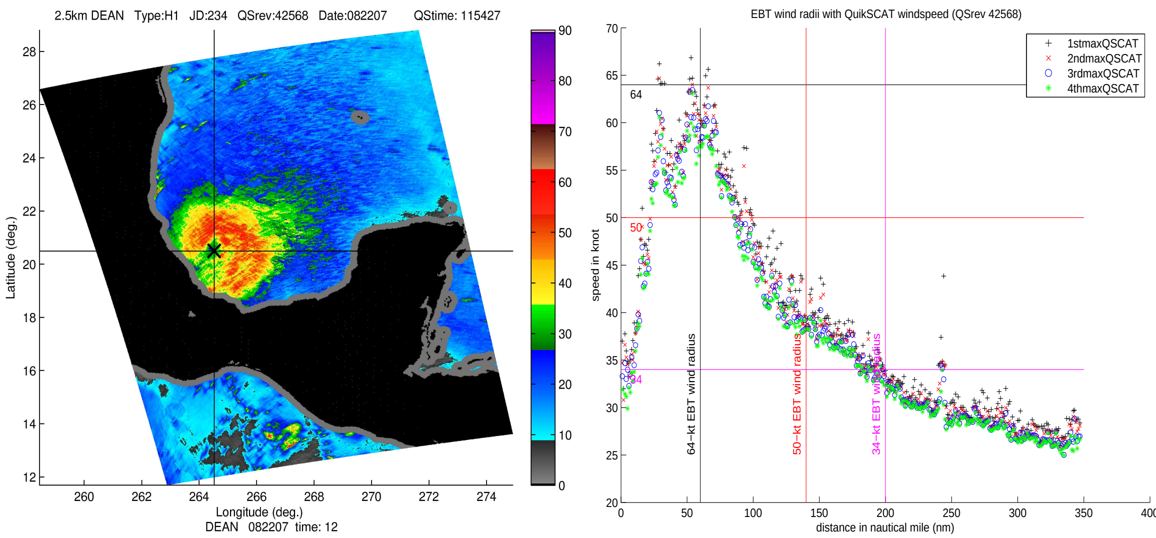

Figure 4.14: H1 Dean on 22 August 2007 at 1154 UTC. The left plot shows QuikSCAT UHR wind speed field only. Note as part of its title the time of QuikSCAT pass over that TC. This can be compared with the time of the collocated estimated wind radii from EBT shown below this plot. The right plot is a scatter plot of the four QuikSCAT wind speed maxima for each distance. The three vertical lines correspond to the three collocated EBT wind radii.

On 14 September 2004 at 1135 UTC, TC Ivan was a hurricane category 2 (see Fig. 4.15). In such an extreme case, it is still possible to obtain good results for the 34- and 50-kt wind radii using QuikSCAT. The 64-kt wind radius, however, is underestimated quite severely. A counterexample is TC Katrina on 28 August 2005 at 1127 UTC (category 5—highest category with sustained wind speed greater than 249 km/hr). Figure 4.16 shows QuikSCAT wind speed field as well as the scatter plot of the four maxima for each distance from the eye overlaid with the three EBT wind radii. This case shows that the three wind radii estimated by QuikSCAT are very close to the EBT wind radii, even in such extreme

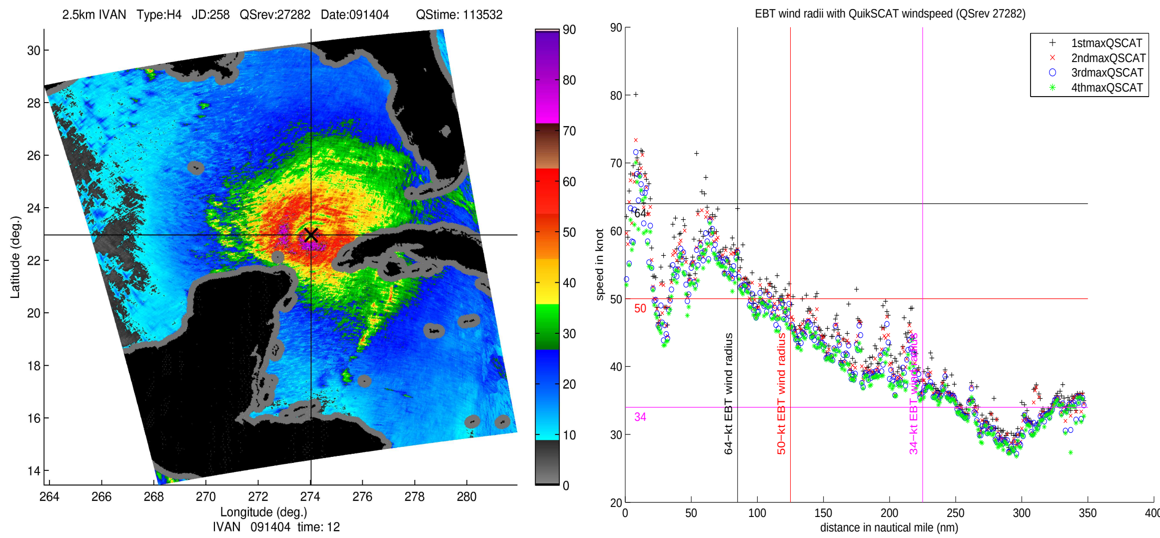

Figure 4.15: H2 Ivan on 14 September 2004 at 1135 UTC. The left plot shows QuikSCAT UHR wind speed field only. Note as part of its title the time of QuikSCAT pass over that TC. This can be compared with the time of the collocated estimated wind radii from EBT shown below this plot. The right plot is a scatter plot of the four QuikSCAT wind speed maxima for each distance. The three vertical lines correspond to the three collocated EBT wind radii.

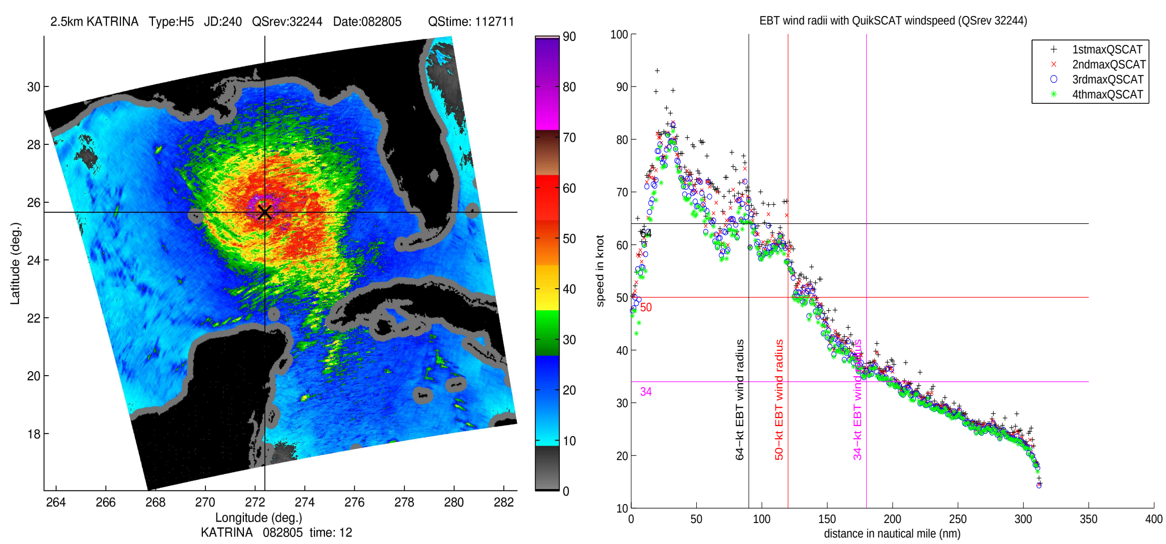

Figure 4.16: H5 Katrina on 28 August 2005 at 1127 UTC. The left plot shows QuikSCAT UHR wind speed field only. Note as part of its title the time of QuikSCAT pass over that TC. This can be compared with the time of the collocated estimated wind radii from EBT shown below this plot. The right plot is a scatter plot of the four QuikSCAT wind speed maxima for each distance. The three vertical lines correspond to the three collocated EBT wind radii.

wind speeds. As mentioned earlier, heavy rain rates may have positively biased QuikSCAT wind speed, but this cannot be confirmed.

4.2.3 Summary

This preliminary analysis has shown the potential of using QuikSCAT UHR wind products to help estimate wind radii. It is important to note that this analysis has been based solely on the use of the four QuikSCAT wind speed maxima for each radius from the eye. These values are noisy and should be used with care. Yet, this data yields a correct 34-kt wind radius most of the time regardless of TC category when compared to both H*wind and EBT. The 50-kt and 64-kt wind radii estimated from QuikSCAT UHR data do not always match either H*wind nor EBT. It has also been observed that rain bands can adversely affect QuikSCAT wind speed estimation. Despite its limitations, it is desirable to use data modeling techniques to estimate QuikSCAT wind radii, which is presented in the following chapter.

Chapter 5

Wind radii estimation using a data modeling technique

The previous chapter evaluates QuikSCAT performance in estimating wind radii based on simple visual analysis. A more sophisticated method is now implemented to estimate wind radii based on a model fit to QuikSCAT data. The purpose of using such a method is to not only automate the wind radii estimation process, but also to provide more objective results. A description of the wind radii estimation procedure is first provided. Detailed explanations of the necessary steps of this process are subsequently described.

5.1 Wind radii estimation procedure

The proposed wind radii estimation procedure is fairly simple and fast to implement. Two major elements constitute the backbone of this estimation process: the use of a static model and a transfer function. First a model based on empirical data from all QuikSCAT TC passes from 1999 to 2007 is used to estimate the mean wind speed versus radius from the eye center location (obtained using interpolated best-track data) for a given TC type. This static model is used to fit wind speed data field from QuikSCAT for TC observations. Since wind radii are reported using one-minute maximum sustained wind speeds (this quantity is defined in Chapter 2 Subsection 2.1.2), a necessary step is implemented to readjust the QuikSCAT model fit wind speed, as QuikSCAT winds are equivalent to a 8-10 minute average wind speed [23]. To this date, H*wind is the only available source of one minute maximum sustained wind speed field. A transfer function based on H*wind collocated TC cases with QuikSCAT is therefore used to adjust the QuikSCAT winds to be compatible with H*wind. This enables the wind radii estimation from a model fit to QuikSCAT data.

5.2 Model fit based on QuikSCAT TC cases from 1999 to 2007

The static model used to fit any wind speed field from QuikSCAT TC cases is based on empirical data from all QuikSCAT TC passes from 1999 to 2007. By compiling all these cases together, noisy measurements (such as under- or overestimated wind speed) may be averaged out. Such model provides a good foundation for accurate and objective wind radii estimation. A description of the model, as well as its performance, is provided in the following subsections. Note that this analysis is done exclusively for the ATL basin, but could be applied in other basins.

5.2.1 Model description

As shown in the previous chapter, the wind speed inferred from QuikSCAT UHR wind products can be under- or overestimated at times due to weather phenomena such as heavy rain and extreme high wind speeds. A model is set up to estimate the mean wind speed at a given radius to help average out noisy measurements for a given data set. The model presented is therefore designed to compute the mean wind speed at each radius from the eye using all QuikSCAT TC passes from 1999 to 2007. The mean wind speed for each distance from the eye is found by computing the conditional expectation $E(S|D = d, Q = q, T = t)$, where S is the wind speed in knots, D is the distance from the eye in nautical miles (nmi), Q is a quadrant, and T is a TC type. Since the conditional expectation $E(S|D = d, Q = q, T = t)$ and all other density functions used to derive this quantity are always conditioned on Q and T throughout this chapter, these two variables are implied to simplify notation (i.e. $f_{S,D|Q,T}(s, d|q, t) \equiv \mathrm{f}_{S,D}(s, d)$). The mean wind speed at each radius from the eye is easily found using the basic definition of empirical conditional expectation as follows:

$$E(S|D = d) = \sum_{s} s \cdot f_{S|D}(s|d), \tag{5.1}$$

where $f_{S|D}(s|d)$ is the conditional density function of the wind speed s given distance d from the eye. To compute $f_{S|D}(s|d)$, it is first necessary to determine the joint density function $f_{S,D}(s, d)$. Figure 5.1 illustrates the joint density functions of wind speed and distance from

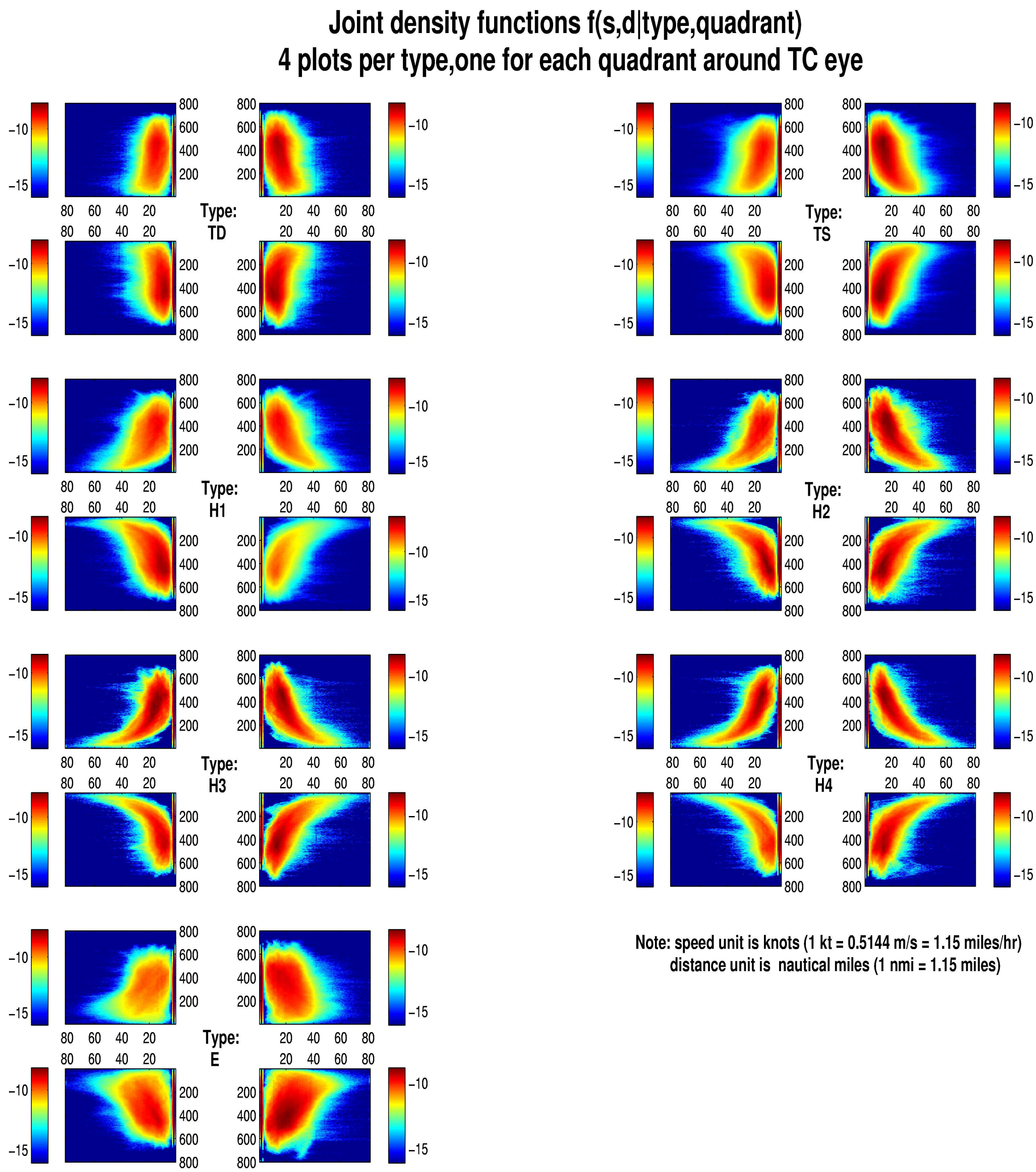

Figure 5.1: Histogram-derived joint density functions of wind speed and distance from the eye. For each TC type, four density plots are shown—one for each quadrant. Color scale is in dB.

the eye for each quadrant and TC type. Note that for a given TC type, the shapes of the joint density functions are very similar from quadrant to quadrant. However, from one TC type to another, there is a definite change in curve shapes. This can be due to significant wind speed changes around the eye's vicinity, and storm size variation between TC types.

Using Bayes' rule, it is possible to find the conditional density function of the wind speed given distance from the eye, $f_{S|D}(s|d)$, as follows:

$$f_{S|D}(s|d) = \frac{f_{D|S}(d|s) \cdot f_S(s)}{f_D(d)} = \frac{f_{S,D}(s,d)}{f_D(d)}. \tag{5.2}$$

Table 5.1 shows the number of cases used per TC type to compute the various density

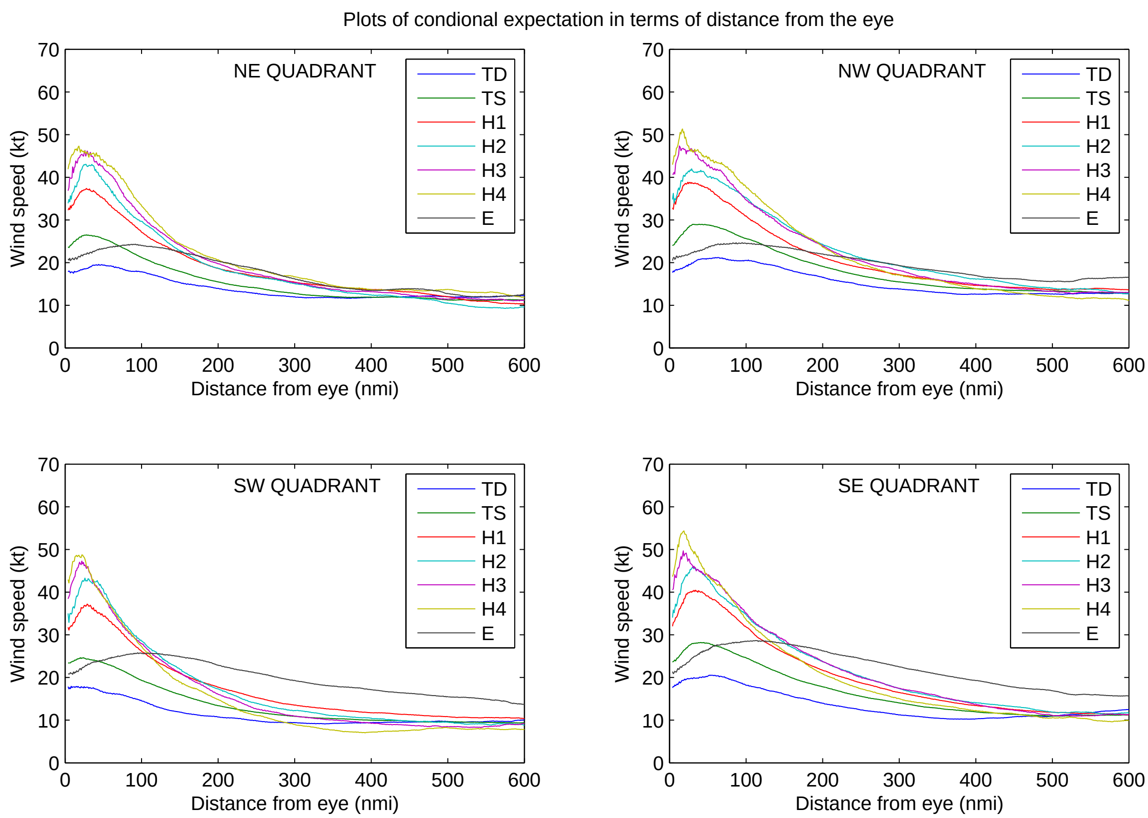

Figure 5.2: Plots of the mean wind speed for each distance or radius from the eye center (one per quadrant). In each plot, seven curves are provided—one per TC type. As expected, peak wind speeds are close to the eye and get higher as TC type varies from TS to H4. Note that type E refers to extra-tropical storms.

functions necessary to ultimately determine the desired conditional expectations. Figure 5.2 shows the plots of the mean wind speed for each distance from the eye (one plot per quad-

Table 5.1: Number of QuikSCAT TC cases used per storm type to generate mean wind speed vs. distance plot (1999 through 2007).

TC type	QuikSCAT TC cases
Tropical Depression	180
Tropical Storm	559
Hurricane Cat 1	214
Hurricane Cat 2	71
Hurricane Cat 3	58
Hurricane Cat 4	61
Extra-tropical	209
Total:	1352

rant). In each plot, seven curves are shown—one per TC type. Note that the smoothest curves represented in Fig. 5.2 correspond to TC types with the most TC cases retrieved as shown in Table 5.1. It is also important to mention the relatively low maxima of the mean wind speed curves shown in Fig. 5.2. The Geophysical Model Function, which relates near-surface wind speed to QuikSCAT backscatter measurements, clips at about 50 ms^{-1}($\approx$ 97.2 knots) [15] and may be a major factor to this limitation. Rain attenuation of high winds may also be a contributor.

5.2.2 Model implementation

Since the model described previously is based on the mean wind speed at a given radius, a linear relationship is assumed between the model fit and the wind speed from the data. Such relationship is shown in the following equation:

$$s_i(d_i) = \alpha + \beta s_m(d_i), \tag{5.3}$$

where $s_i(d_i)$ and $s_m(d_i)$ represent the data wind speed and the model wind speed, respectively, at distance d_i from the eye. α and β represent the model parameters which control the shape and vertical shift of the model fit curve. These parameters can be found using the minimum mean square error estimation technique (MMSE). Once α and β are determined, a model fit to the data is possible using the estimated mean wind speed.

Rewriting Eq. 5.3 in matrix form as follows is helpful to understand how to use the MMSE technique to estimate the wind speed:

$$\begin{pmatrix} s_1(d_1) \\ .. \\ s_i(d_i) \end{pmatrix} = \begin{pmatrix} 1 & s_m(d_1) \\ .. & .. \\ 1 & s_m(d_i) \end{pmatrix} \cdot \begin{pmatrix} \alpha \\ \beta \end{pmatrix} \equiv \underline{S} = \underline{D} \cdot \underline{A}. \tag{5.4}$$

The model parameters α and β (in $\underline{A}$) can be found using the pseudo-inverse technique:

$$\underline{A} = (\underline{D}^T \cdot \underline{D})^{-1} \cdot \underline{D}^T \cdot \underline{S}. \tag{5.5}$$

This provides a minimum mean square error solution to the system of linear equations as shown in Eq. 5.4, and a model fit to the data is obtained when $\underline{A}$ is found.

5.2.3 Preliminary results

Figure 5.3 shows a scatter plot of the wind speed versus radius from the eye in the NE quadrant of TC Noel in 2007. In this plot, the model fit is overlaid with the data from QuikSCAT UHR wind speed. Note that the model fit is surely averaging out noisy measurements from the data. Assuming the estimation of a wind radius for a given wind speed requires the knowledge of the maximum wind speed at each radius from the eye, it is necessary to modify our model fit since this latter is currently based on mean wind speeds. To resolve this issue, the standard deviation of our mean wind speed model is thus added at each radius. Figure 5.4 shows an updated scatter plot of the wind speed versus radius from the eye for TC Noel in 2007, with the original model fit curve and the model fit curve with the standard deviation added. The latter curve should be a stronger foundation to help in the process of wind radii estimation.

As mentioned in section 5.1, it is important to remind that best-track wind radii are estimated based on 1-minute maximum sustained wind speeds, while QuikSCAT wind speed is roughly equivalent to a 8-10 minute mean surface wind [23]. Therefore, it is necessary to adjust QuikSCAT wind speed to be consistent with a 1-minute maximum sustained wind speed prior to estimating wind radii from it.

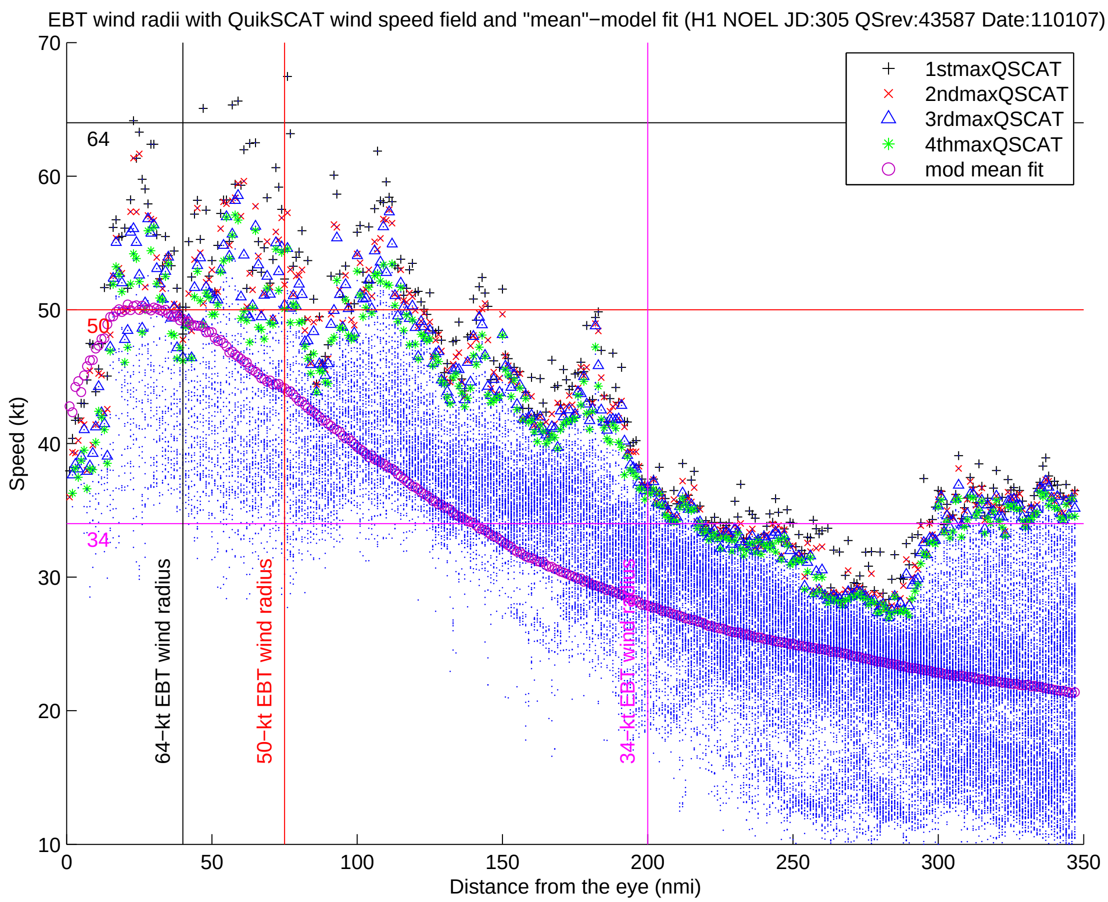

Figure 5.3: Scatter plot of QuikSCAT wind speed (kt) versus distance (nmi) from the eye for TC Noel on 1 January 2007 at 2335 UTC. A 'mean' model fit is overlaid to the data. EBT wind radii are also provided in this scatter plot.

5.3 Bias adjustment using H*wind data on model fit implementation

H*wind data provide a 1-minute maximum sustained wind speed field for each available TC collocation with QuikSCAT data. To ensure data compatibility, it is of interest to use all H*wind and QuikSCAT TC collocations to perform a bias adjustment on the model fit wind speed based on H*wind wind speed. Figure 5.5 shows H*wind versus the estimated wind speed (from the updated model fit) scatter plots for the 47 collocations found (see Table 4.1). The first five plots (from upper left to bottom left) show H*wind and model wind speeds for various distance ranges from the eye. These plots show that for distances close to the eye (10-60 nmi), the model fit based on mean wind speed plus standard deviation generally underestimates wind speed. As distance from the eye increases, the model fit

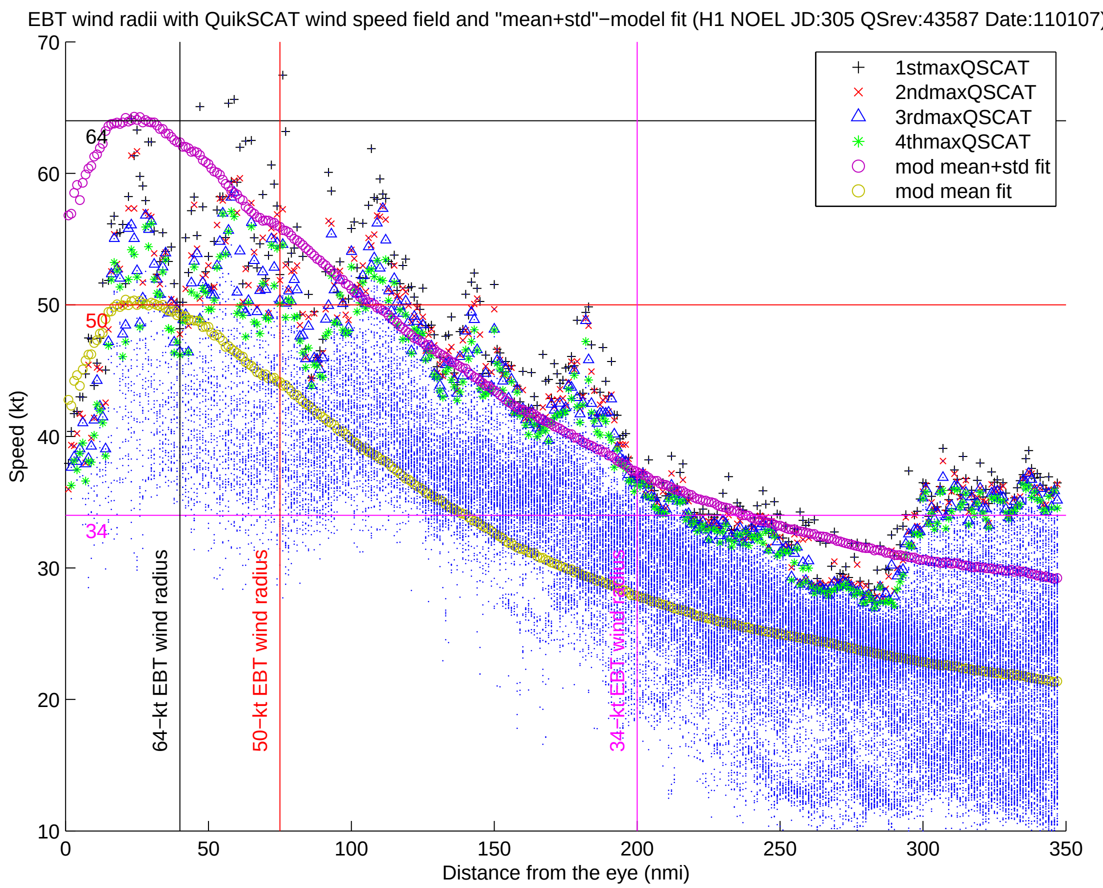

Figure 5.4: Scatter plot of QuikSCAT wind speed (kt) versus distance (nmi) from the eye for TC Noel on 1 January 2007 at 2335 UTC. A 'mean+std' model fit is overlaid to the data. EBT wind radii are also provided in this scatter plot.

slowly overestimates wind speed. The last plot in Fig. 5.5 has all five previous scatter plots overlaid with a second order fit. The coefficients of the second order fit are used to adjust the QuikSCAT model fit wind speed. Figure 5.6 shows H*wind wind speed versus the adjusted QuikSCAT model fit wind speed. A higher correlation is found between the two sets of data for all distances from the eye. Yet, for distances closer to the eye (see upper left scatter plot of Fig. 5.6), correlation is lower for extremely high wind speed which is to be expected due to the GMF clipping at about 98 knots (50 m/s). Using the adjusted version of the model fit based on mean wind speed plus standard deviation, it is possible to estimate wind radii.

5.3.1 QuikSCAT wind radii validation

The wind radii estimation process described in this chapter can be easily implemented. Next, it is necessary to evaluate its performance. The only known ground truth wind radii data source comes from the Extended Best-Track dataset [21]. Unfortunately, only 39 temporal and spatial collocations (including the following TC types: TS, H1-2-3-4, E) have been identified between QuikSCAT and EBT dataset between 1999 and 2007. Figure 5.7 shows the scatter plot of 34-, 50-, and 64-kt wind radii from both QuikSCAT adjusted model fit and EBT. Results obtained from QuikSCAT adjusted model fit are generally highly correlated with EBT estimated wind radii. It is interesting to note that there are less missed 64-kt than 50-kt wind radii estimated from QuikSCAT (6 versus 15—see Fig. 5.7). Despite the number of missed wind radii, we can conclude that it may be possible to estimate any wind radius in an automated fashion using the procedure outlined in this chapter. Once wind radii are found, they can be analyzed and adjusted if necessary by hurricane forecasters based on their extensive experience.

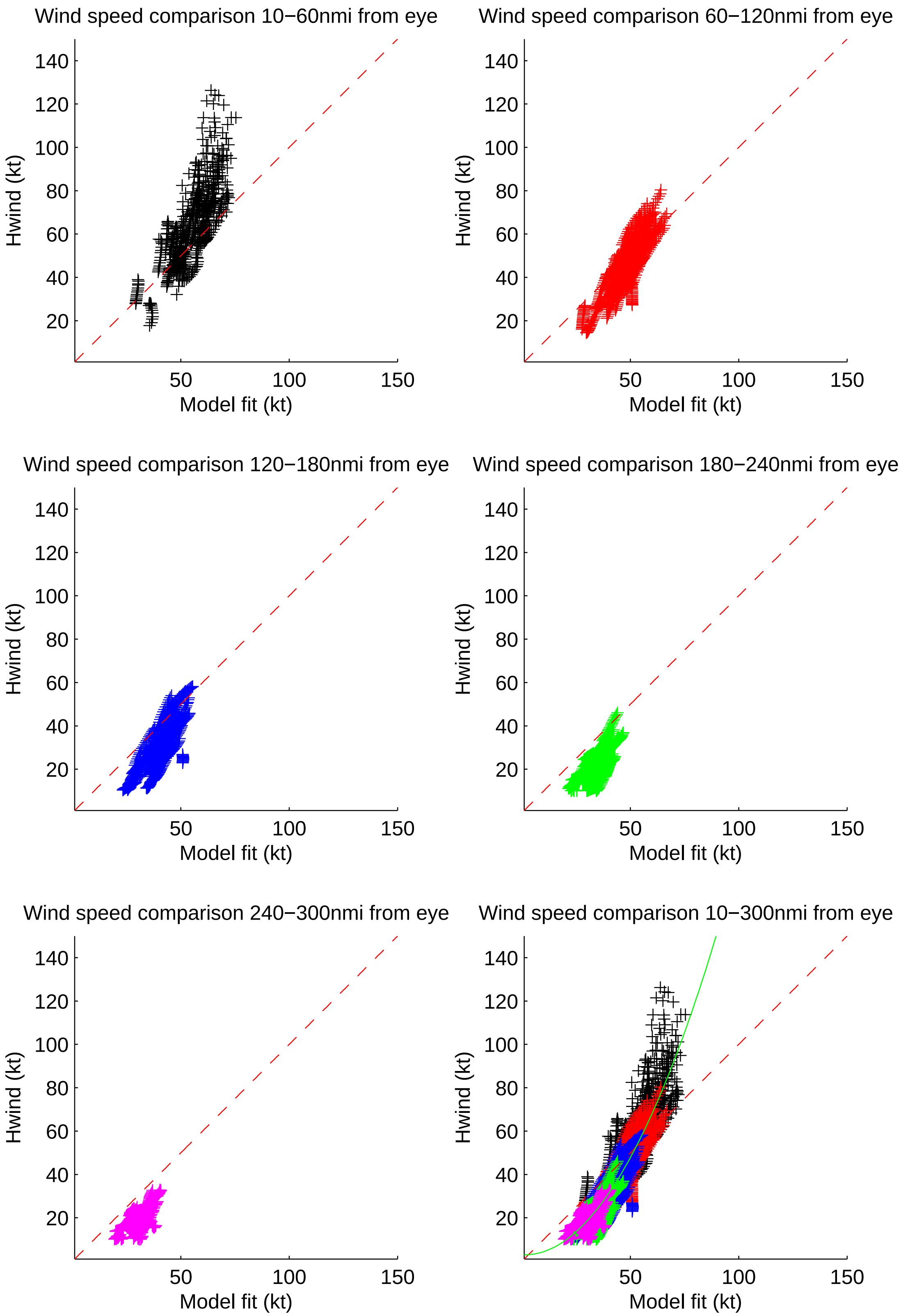

Figure 5.5: H*wind versus QuikSCAT wind speed scatter plots at various distance ranges from the eye. Note the second order fit on the last plot (see bottom right plot). Wind speed is in knots.

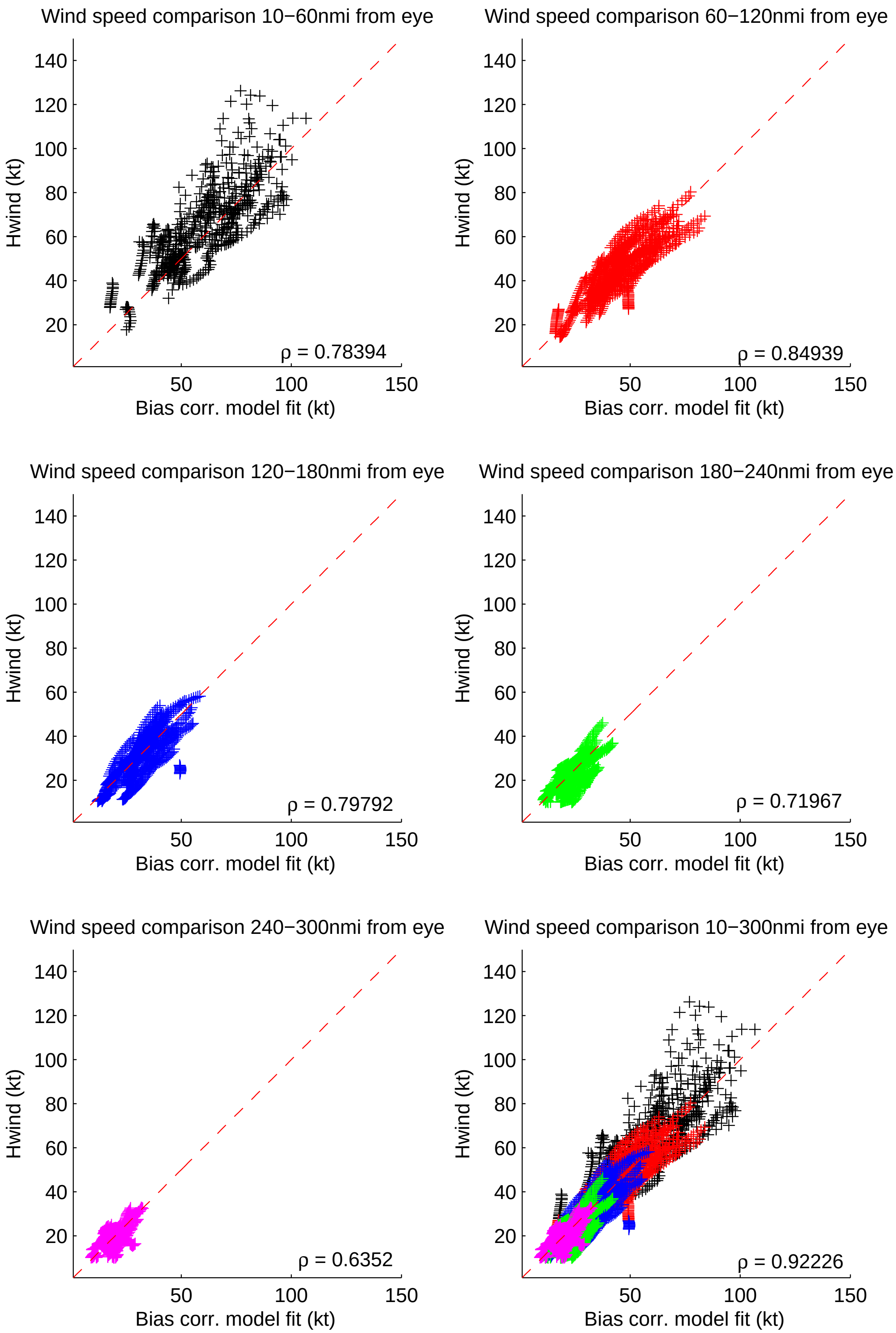

Figure 5.6: H*wind versus QuikSCAT adjusted wind speed scatter plots at various distance ranges from the eye. Wind speed is in knots.

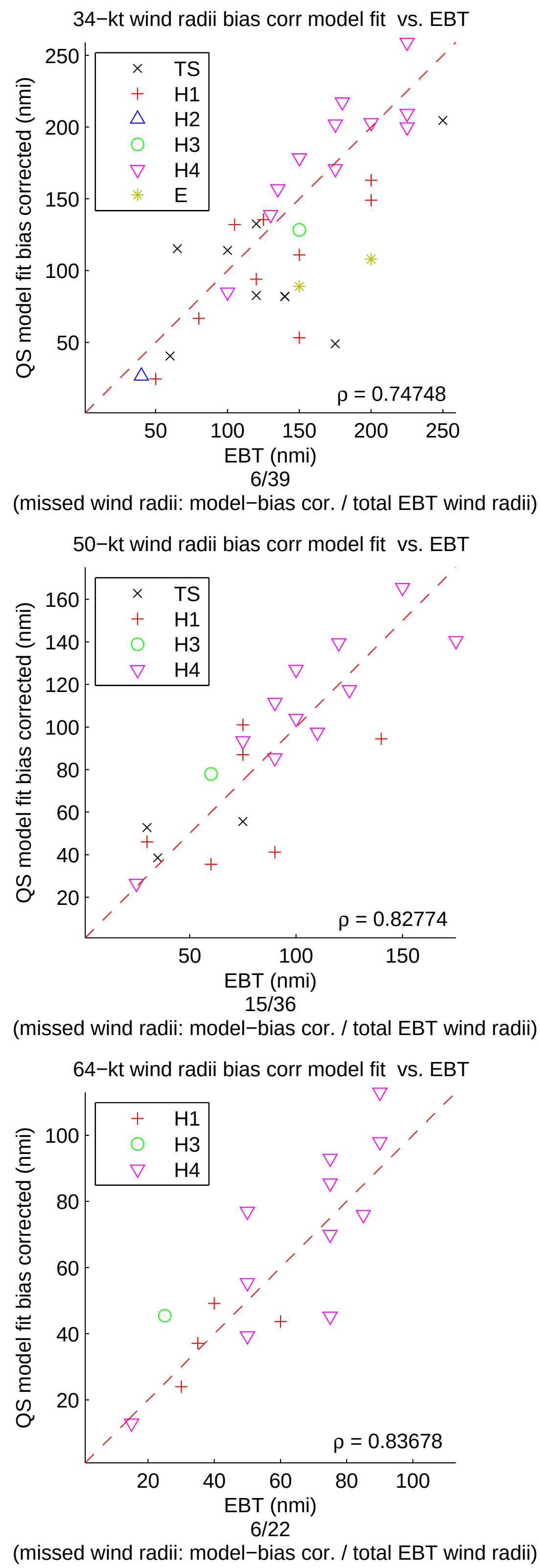

Figure 5.7: Scatter plots of 34-, 50-, and 64-kt wind radii from QuikSCAT adjusted model fit versus EBT. At the bottom of each scatter plot, the number of missed QuikSCAT model fit wind radii is specified. In the lower right corner of each plot, a correlation coefficient ρ is also provided.

Chapter 6

Conclusion

This thesis provides an analysis of QuikSCAT UHR wind product's effectiveness in estimating specific TC parameters such as storm eye location and wind radii. In Chapter 3, QuikSCAT TC UHR passes are visually analyzed and separated into two categories (low and high confidence) depending on the confidence level of identifying TC eye location. This analysis is done by strictly relying on the wind speed and direction fields. TC eye identification using high confidence cases provide similar results compared to best track data. A high confidence UHR image is therefore useful to obtain a good estimate of a TC eye location. It can be argued however that QuikSCAT data is not necessary to identify eye location when storms are well defined since the eye can be identified using infrared or optical satellite imagery. The eye of the storm, on the other hand, can at times be covered by high altitude clouds, called the Central Dense Overcast (CDO), which makes it impossible to find the eye using traditional methods. In such cases, QuikSCAT data can be essential.

Identifying TC eye center in a low confidence case (under-developed TC or TC with a poorly defined eye) can be difficult, and QuikSCAT wind products are considered useful in identifying developing tropical depressions [10]. Though poor results in determining TC eye location are generally obtained with low confidence QuikSCAT images, these images are still valuable to the weather community.

Chapters 4 and 5 describe and analyze two ways of estimating wind radii using QuikSCAT UHR data. The first method consists of a direct wind radius estimation from QuikSCAT maximum wind speed at a given radius. This estimation is compared with both H*wind and EBT collocated TC cases. The second method proposes the use of a static model and a transfer function applied to QuikSCAT UHR wind product to automatically estimate wind radii for any TC. The method proposed is straightforward and easy to implement. Validation of the results is performed with collocated EBT cases. These results demonstrate that QuikSCAT UHR wind product can be used to estimate wind radii. The automated method assumes knowledge of the eye center location and the storm intensity to use the appropriate static model. In a near-real time application, the eye center location would have to be identified manually beforehand. Once the latter is estimated, a hurricane forecaster can infer a wind radius estimate from QuikSCAT UHR wind product and adjust it if necessary. It is important to note that it is only possible to obtain a wind radius estimate from QuikSCAT a maximum of twice a day due to the nature of QuikSCAT daily ocean coverage; whereas wind radii are to be reported every six hours as part of the official NHC forecast advisories during a storm lifetime. Even with the limited daily coverage QuikSCAT can provide for a given TC, its UHR wind product may be the only reliable source to estimate a TC wind speed field when storms are out of reach from jet aircraft.

6.1 Contributions

To this date, there has been no comprehensive report on the effectiveness of using QuikSCAT UHR wind product in TC analysis. This thesis provides such a report. Comparison between L2B and UHR wind products in identifying TC eye center locations has been done in [4]. The comparison has not been conducted, however, with the use of a confidence flag. The use of such a flag shows more explicitly the effectiveness of using UHR images in TC eye center identification.

Another contribution found in this thesis is an in-depth analysis of QuikSCAT TC observation reliability (see Chapter 3 Section 3.4). This is the first published analysis. Finally, an algorithm has been developed to automatically compute a wind radius for a given quadrant of a given TC, using UHR wind product exclusively. While results presented in Chapter 5 are promising, further work is possible.

6.2 Future work

The current limitation of QuikSCAT UHR wind product in TC research is QuikSCAT's degraded performance in high rain rate areas, extreme wind conditions, and close to land boundaries. These extreme weather conditions almost always accompany any TC. Measurements are noisier in these conditions and thus not reliable. It is therefore important to improve QuikSCAT backscatter measurements in such weather conditions to increase the estimation accuracy of the TC parameters discussed in this thesis.

The following three methods propose interesting approaches in enhancing QuikSCAT backscatter measurement' quality and use:

- In [24], an algorithm is described and used to remove land contamination and improve the ability to retrieve coastal winds by as much as 25 km using QuikSCAT UHR wind product. Implementing this technique would enable more accurate wind radius estimates when TC are over groups of islands or close to coastal areas. It may also simplify TC eye center identification in such situations.

- Backscatter response in high rain rate conditions can be adjusted using a simultaneous wind and rain retrieval technique, which enables the adjustment of the GMF to account for rain effects [25]. As a result, wind speeds inferred from QuikSCAT would be closer to the true values especially in areas of both significant rain rate and high or low wind speed.

- [26] discusses a method to improve wind direction estimates and to reduce variability in wind speed estimates in hurricanes. This technique ultimately avoids cross track winds obtained in areas of extreme high wind speed and high rain rate commonly found around the eye vicinity, resulting in less ambiguous TC eye center identification.

A new set of UHR wind product can be created by combining the three methods presented in [24], [25], and [26]. TC eye identification and wind radii estimation can be improved by re-conducting the analysis proposed in this thesis using the new resulting UHR dataset.

To this date, it is not clear to the author which QuikSCAT wind products (i.e. L2B or UHR) NHC forecasters use in their operational TC wind radii estimation process, though a recent report does mention the use of L2B wind product only [27]. Furthermore, it is not certain the significance of the role QuikSCAT plays in the wind radii estimation process at NHC. It is of interest to collaborate with NHC forecasters and present our wind radii estimation results based exclusively on UHR wind product. This is a good way to show to NHC forecasters the apparent effectiveness of using QuikSCAT in estimating these TC parameters.

Bibliography

[1] National Oceanic and Atmospheric Administration (NOAA), "Hurricane basics," http://hurricanes.noaa.gov/pdf/hurricanebook.pdf, May 1999. [Online]. Available: http://hurricanes.noaa.gov/pdf/hurricanebook.pdf 1, 6

[2] AMS Council, "Hurricane Forecasting in the United States," http://www.ametsoc.org/POLICY/2007hurricaneforecasting.html, May 2009. 1

[3] D. Long, J. Luke, and W. Plant, "Ultra high resolution wind retrieval for SeaWinds," in *International Geoscience and Remote Sensing Symposium*, Toulouse, France, July 2003, pp. 1264–1266. 2, 13, 18

[4] R. Ryan Halterman, "Observation and tracking of tropical cyclones using resolution enhanced scatterometry," Master's thesis, Brigham Young University, October 2006. 2, 68

[5] R. Simpson, R. Anthes, M. Garstang, and J. Simpson, Eds., *Hurricane! Coping with Disaster: Progress and Challenges since Galveston, 1900.* American Geophysical Union, 2003. 5, 6

[6] C. Weatherford and W. M. Gray, "Typhoon structure as revealed by aircraft reconnaissance. Part II: Structural variability," *Monthly Weather Review*, vol. 116, pp. 1044–1056, 1988. [Online]. Available: http://ams.allenpress.com/archive/1520-0493/116/5/pdf/i1520-0493-116-5-1044.pdf 6, 22

[7] Cooperative Program for Operational Meteorology, Education and Training (COMET Program), "Structure of airflow around the eye of a hurricane," http://www.comet.ucar.edu/, March 2009. 7

[8] *Interagency Strategic Research Plan for Tropical Cyclones: The Way Ahead.* Office of the Federal Coordinator for Meteorological Services and Supporting Research, 2007, ch. Current capabilities and limitations. 8

[9] G. K. Davis, "History of the NOAA program," *Journal of Applied Remote Sensing*, vol. 1, January 2007. 8

[10] K. B. Katsaros, E. B. Forde, P. Chang, and W. T. Liu, "QuikSCAT's SeaWinds facilitates early identification of tropical depressions in 1999 hurricane season," *Geophysical Research Letters*, vol. 28, no. 6, pp. 1043–1046, March 2001. 9, 67

[11] F. T. Ulaby, R. K. Moore, and A. K. Fung, *Microwave Remote Sensing: Active and Passive Volume II: Microwave Remote Sensing Fundamentals and Radiometry*, D. S. Simonett, Ed. Addison-Wesley, 1982. 10

[12] F. M. Naderi, M. H. Freilich, and D. G. Long, "Spaceborne Radar Measurement of Wind Velocity Over the Ocean—An Overview of the NSCAT Scatetterometer System," *Proceedings of the IEEE*, vol. 79, no. 6, pp. 850–866, June 1991. 10

[13] R. N. Hoffman and S. M. Leidner, "An Introduction to the Near-Real-Time QuikSCAT Data," *Weather and Forecasting*, vol. 20, no. 4, pp. 476–493, August 2005. 12

[14] M. W. Spencer, C. Wu, and D. G. Long, "Improved Resolution Backscatter Measurements with the SeaWinds Pencil-Beam Scatterometer," *IEEE Transactions on Geoscience and Remote Sensing*, vol. 38, no. 1, pp. 89–104, 2000. xiii, 12

[15] T. Lungu, *QuikSCAT Science Data Product User's Manual: Overview and Geophysical Data Products, version 3.0*, Jet Propulsion Lab., Pasadena, Calif., June 2006. [Online]. Available: ftp://podaac.jpl.nasa.gov/pub/ocean_wind/quikscat/doc/QSUG_v3.pdf 13, 59

[16] J. M. Von Ahn, J. M. Sienkiewicz, and P. S. Chang, "Operational impact of QuikSCAT winds at the NOAA ocean prediction center," *Weather and Foreacsting*, vol. 21, no. 4, pp. 523–539, 2006. 13

[17] D. Long, "Ultra high resolution rain retrieval from QuikSCAT data," in *International Geoscience and Remote Sensing Symposium*, Denver, Colorado, August 2006, pp. 4113–4116. 18

[18] Hurricane Hunters Association, "The Mission of the Hurricane Hunters," http://www.hurricanehunters.com/mission.html, May 2009. 35

[19] M. D. Powell, S. H. Houston, L. R. Amat, N Morisseau-Leroy, "The hrd real-time hurricane wind analysis system," *J. Wind Engineer. and Indust. Aerodyn.*, vol. 7778, 1998. 36

[20] Central Florida Remote Sensing Lab, Deparment of Atmospheric Sciences, UNC Asheville, "Nasa Ocean Vector Winds," http://cyclone.atms.unca.edu/quikscat/hwind.html, April 2008. 36, 37

[21] STAR Center for Applications and Research, "Mark demaria cooperative research program," http://www.star.nesdis.noaa.gov/star/DeMaria_M.php, May 2009. 48, 63

[22] "Risk prediction initiative," http://w3.bios.edu/rpi/rpihome.html, May 2009. 48

[23] Remote Sensing Systems, "Description of scatterometer data products," http://www.ssmi.com/qscat/qscat_description.html, February 2009. 55, 60

[24] M. P. Owen and D. G. Long, "Land-contamination compensation for quikscat near-coastal wind retrieval," *IEEE Transactions on Geoscience and Remote Sensing*, vol. 47, no. 3, pp. 839–850, March 2009. 69

[25] M. P. Owen and D. G. Long, "Progress toward validation of quikscat ultra-high-resolution rain rates using trmm pr," in *International Geoscience and Remote Sensing Symposium*, Boston, Massachusetts, July 2008, pp. 299–302. 69

[26] B. A. Williams and D. G. Long, "Estimation of Hurricane Winds From SeaWinds at Ultrahigh Resolution," *IEEE Transactions on Geoscience and Remote Sensing*, vol. 46, no. 10, pp. 2924–2935, October 2008. 69

[27] M. J. Brennan, C. C. Hennon, and R. D. Knabb, "The Operational Use of QuikSCAT Ocean Surface Vector Winds at the National Hurricane Center," *Weather and Forecasting*, vol. 24, pp. 621–645, June 2009. 69